

***Operando* measurement of ethanol steam reforming reaction on Ni(111) using ambient pressure X-ray photoelectron spectroscopy**

Susumu Yamamoto^{1,2}, Kota Moriyama³

¹ *International Center for Synchrotron Radiation Innovation Smart (SRIS), Tohoku University*

² *Institute of Multidisciplinary Research for Advanced Materials (IMRAM),
Tohoku University*

³ *Department of Electrical, Information and Physics Engineering, School of Engineering,
Tohoku University*

Ethanol steam reforming (ESR) reaction, which produces hydrogen from ethanol ($\text{CH}_3\text{CH}_2\text{OH}$ (EtOH) + $3\text{H}_2\text{O} \rightarrow 2\text{CO}_2 + 6\text{H}_2$), has attracted much attention toward the realization of a hydrogen society. However, the reaction mechanism of the ESR reaction is not fully understood. This is mainly because there are many side reactions in the ESR reaction, which produce various molecules such as CH_4 , C_2H_4 , CO . To elucidate the reaction path and reaction mechanism of the ESR reaction, we performed *operando* measurements of the ESR reaction using ambient pressure X-ray photoelectron spectroscopy (AP-XPS).

The experiments were performed using the AP-XPS system installed at SPring-8 BL07LSU [1-4]. The Ni(111) surface was cleaned by a cycle of Ar^+ ion sputtering and annealing, and used as a catalyst for the ESR reaction. The Ni(111) catalyst was placed in the mixed gas atmosphere of 3 mbar EtOH and 9 mbar H_2O , and was heated from 300 K to 700 K. For comparison, the Ni(111) catalyst was heated in the pure gas atmosphere of 3 mbar EtOH (or 9 mbar H_2O). The catalytic activity was monitored by mass spectrometry (MS), and the surface chemical states and surface adsorbed molecules of the Ni catalyst were measured by AP-XPS.

Figure 1 shows the catalytic activity of Ni(111) in the mixed gas of EtOH and H_2O as a function of temperature. At 600-700 K, the formation of H_2 and CO_2 is confirmed. The MS and AP-XPS results for EtOH + H_2O and pure EtOH were almost identical. This indicated that EtOH decomposition, one of the elementary processes of the ESR reaction, was the dominant process in the current reaction conditions. Furthermore, in the Ni $2p$ AP-XPS spectra, the Ni surface was oxidized only when EtOH was introduced, and the surface oxidation/reduction coincided with EtOH introduction/decomposition, indicating that EtOH acts as an oxidant on the Ni surface.

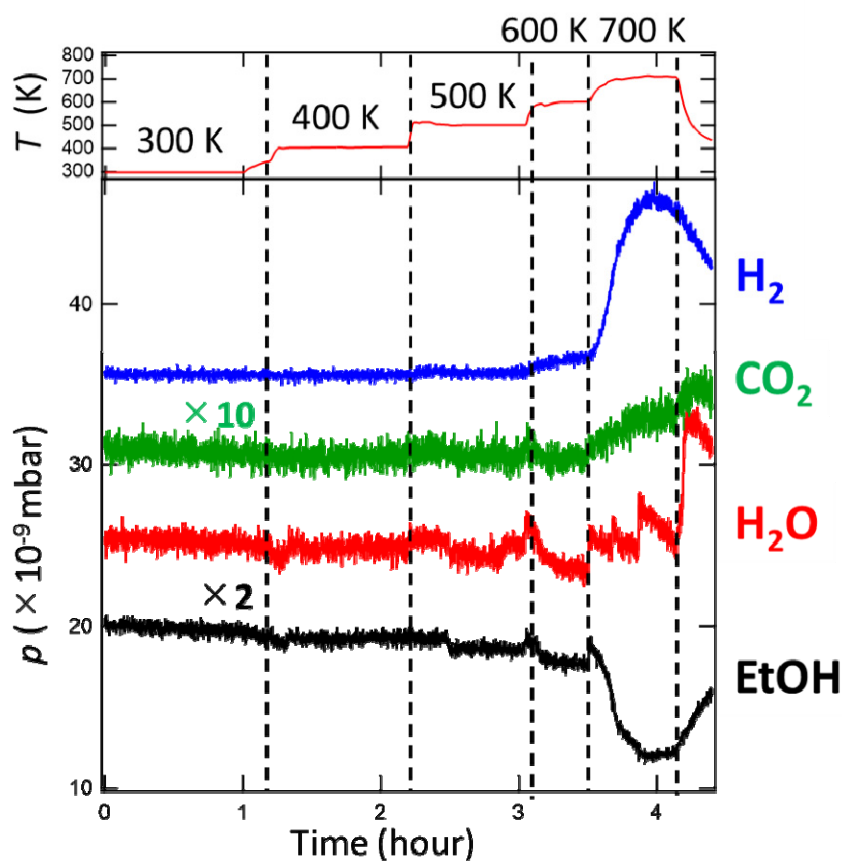


Figure 1. Catalytic activity measurements of Ni(111) for an ESR reaction. Gas composition was monitored with mass spectrometer, while the Ni catalyst was heated in a stepwise manner from 300 K to 400 K, 500 K, 600 K and 700 K in the mixed gas of 3 mbar EtOH and 9 mbar H₂O.

REFERENCES

- [1] T. Koitaya, S. Yamamoto *et al.*, *Topics in Catalysis* **59**, 526-531 (2016).
- [2] T. Koitaya, S. Yamamoto *et al.*, *e-J. Surf. Sci. Nanotechnol.* **17**, 169-178 (2019).
- [3] S. Yamamoto *et al.*, *Synchrotron Radiat. News*, in press (2022).
- [4] S. Yamamoto *et al.*, *Journal of the Japanese Society for Synchrotron Radiation Research* **35**, 182-190 (2022). (in Japanese)

DEVELOPMENT OF SOFT X-RAY MICROSCOPY SYSTEM WITH CYLINDRICAL-SHAPE WOLTER MIRROR

Takashi KIMURA,¹ Yoko TAKEO,^{1,2} Kai SAKURAI,³ Noboru FURUYA,³
Satoru EGAWA,⁴ Gota YAMAGUCHI,⁵ Yusuke MATSUZAWA,⁶ Takehiro KUME,⁶
Hidekazu MIMURA,⁷ Mari SHIMURA,⁸ Haruhiko OHASHI,^{2,5}
Iwao MATSUDA,¹ and Yoshihisa HARADA¹

¹*The Institute for Solid State Physics, The University of Tokyo*

²*Japan Synchrotron Radiation Research Institute*

³*Department of Applied Physics, School of Engineering, The University of Tokyo*

⁴*RIKEN Center for Advanced Photonics*

⁵*RIKEN, SPring-8 Center, 1-1-1*

⁶*Technology Center, Natsume Optical Corporation*

⁷*Department of Precision Engineering, School of Engineering, The University of Tokyo*

⁸*Research Institute, National Center for Global Health and Medicine*

X-ray microscopy has a wide range of applications in science due to its high spatial resolution and variety of analytical techniques. Ptychography provides a particularly high spatial resolution by reconstructing the sample image using phase recovery calculations[1, 2]. The combination of ptychography and spectroscopy in the soft X-ray region is promising for investigating samples with light-element-rich heterogeneous structures. For example, in the combination of soft X-ray ptychography with X-ray absorption spectroscopy, mapping the chemical state of magnetic nanoparticles in bacteria[3] and the visualization of the cathode degradation mechanism of the lithium-ion batteries[4] have been demonstrated.

For ptychography at multiple X-ray wavelengths, total reflection mirror optics have the optimal character of achromatic aberration and high focusing efficiency. The current achievable focusing size of total reflection mirrors in soft X-rays is around a few hundred nanometers[5], much larger than that of zone plates. However, the spatial resolution obtained in ptychography is independent of the focusing beam size, which makes the total reflection mirrors a potential candidate. In addition, the long working distance of the mirror optics also makes it suitable for applications in tomographic and in-situ/operand measurements.

In this work, we developed a new total-reflection Wolter mirror optics for soft X-ray ptychography and demonstrated that it can be used to measure cellular samples[6]. The total-reflection Wolter mirror was fabricated by modifying our previous precision electroforming process. The reflecting surface of the Wolter mirror, which was covered with Au, enables seamless ptychographic measurements in a wide energy range of soft X-rays. Figure 1 shows the schematic illustration of the system

A soft X-ray ptychographic system with a total-reflection Wolter mirror achieved a resolution of approximately 50 nm in a test chart evaluation. We have also shown that it is possible to visualize the microstructure of a mammalian cell over a wide photon energy range without chromatic aberration. Figure 2 shows the retrieved image of the mammalian cell from 250 eV to 1.2 keV. Furthermore, taking advantage of the long working distance of the optical system, stereo imaging with a large rotation angle was also attempted to measure the cell sample. Ptychographic imaging with a pink beam from the undulator was also possible. The soft X-ray ptychography system based on the Wolter mirror optics developed in this study is expected to be highly effective for investigating thick samples with complex three-dimensional structures and chemical compositions.

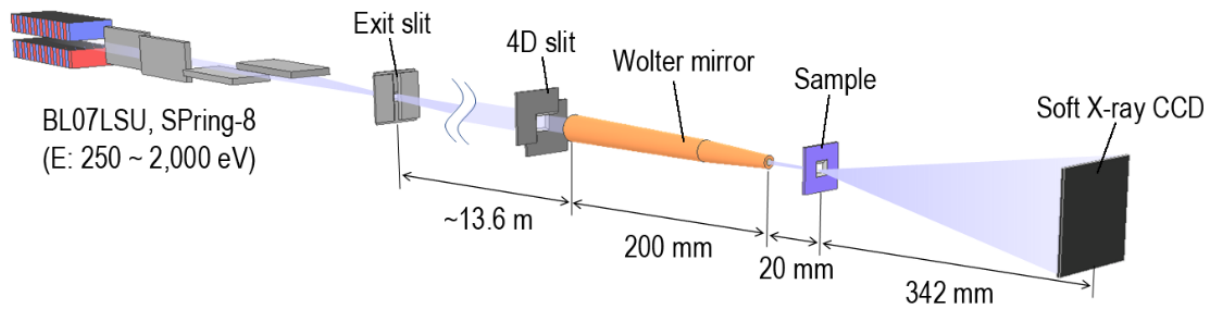


Figure 1. Schematic illustration for the soft X-ray ptychography system at BL07LSU of SPring-8.

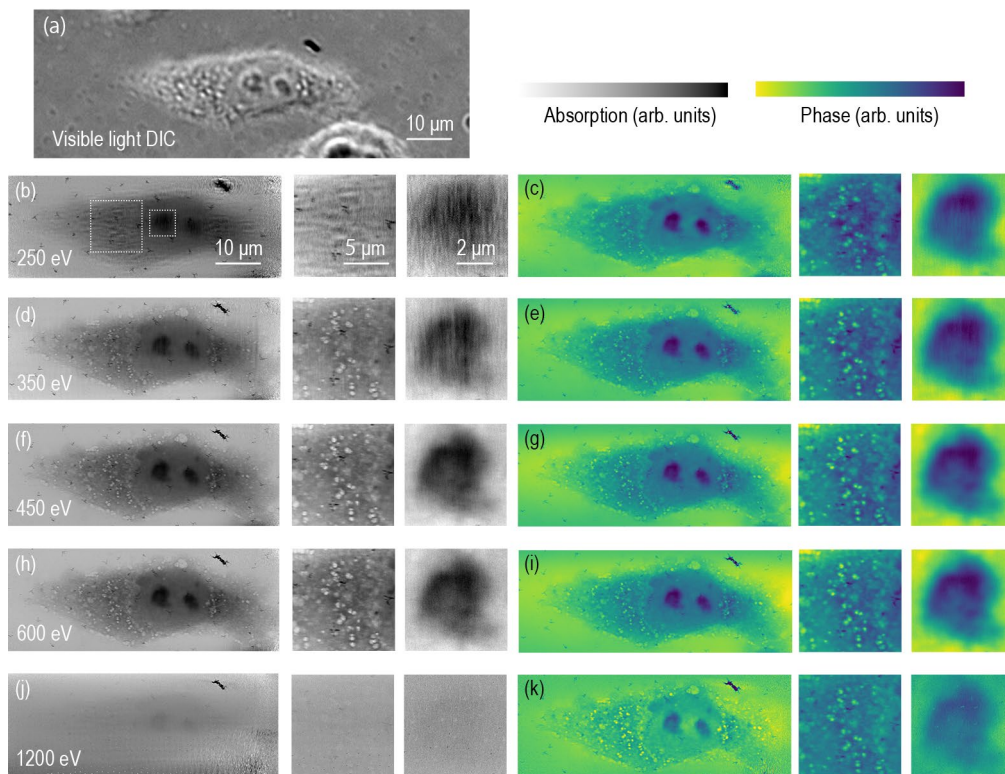


Figure 2. Soft X-ray ptychography measurement of a mammalian cell. (a) Visible light differential interference contrast image. (b-k) Reconstructed absorption (b,d,f,h,j) and phase (c,e,g,i,k) images at 250 eV, 350 eV, 450 eV, 600 eV, and 1200 eV. The magnified images to the right of the main images are taken from areas corresponding to the dotted rectangles shown in (b).

REFERENCES

- [1] A. M. Maiden, J. M. Rodenburg, *Ultramicroscopy*, 109 (10), 1256 (2009).
- [2] P. Thibault, et al., *Science*, 321, 379 (2008).
- [3] X. Zhu, et al. *Proc. Natl. Acad. Sci.*, 113 (51) E8219 (2016).
- [4] T. Sun, et al., *ACS Nano*, 15, 1475 (2021).
- [5] Y. Takeo, et al., *Appl. Phys. Lett.* 117, 151104 (2020)
- [6] T. Kimura, et al., *Opt. Express*, accepted.

A NOVEL MEASUREMENT METHOD OF NEAR-EDGE X-RAY ABSORPTION FINE STRUCTURE USING CONTINUOUS ROTATION OF LINEAR POLARIZATION ANGLES

Masafumi HORIO¹, Yoshiki KUDO¹, Yasuyuki HIRATA², Masahito NIIBE³,
Masato KOTSUGI⁴, Iwao MATSUDA¹

¹*The Institute for Solid State Physics, The University of Tokyo*

²*Department of Applied Physics, National Defence Academy*

³*Laboratory of Advanced Science and Technology for industry, University of Hyogo*

⁴*Department of Materials Science and Technology, Tokyo University of Science*

Near-edge X-ray absorption fine structure (NEXAFS) is one of the X-ray spectroscopy methods employed to analyze the electronic state [1]. In recent years, NEXAFS measurements have evolved into nano-spatial imaging and *operando* experiments, allowing, for example, to identify orbital types and determine molecular configurations by use of linear polarization. In such measurements, NEXAFS spectra are acquired by changing the angle between the molecule and the linear polarization. Typically, at a synchrotron radiation facility, the linear polarization of the beam is fixed, and a series of angle-resolved data is collected while the sample is rotated. This experimental method is simple, but at the same time, it limits the conditions of the sample environment. For example, the sample must be uniform to cover the misalignment between the beam spot and the sample rotation axis. On the other hand, in the case of nano-beam NEXAFS and *operando* experiments, it is technically difficult to ensure the exact beam position after sample rotation on a non-uniform and complex nanodevice. Therefore, it is now required to rotate the linear polarization of the X-ray beam instead of rotating the sample. In the present research, we designed a novel control method of linear polarization angles by the segmented undulator of SPring-8 BL07LSU.

The light source of SPring-8 BL07LSU consists of an 8-segment insertion device (ID) and a 7-segment phase shifter (PS), as shown in Fig. 1 [2]. The ID segments are either horizontal or vertical figure-8 undulators. The horizontal (H) and vertical (V) ID segments are alternately placed between the PS, which is used to adjust the relative phase of the radiation. To achieve linear polarization at arbitrary angles, two waves of left and right circular polarization produced by sets A and B of ID segments were combined, as shown in Fig. 1 (b). Set A consists of H1, V2, H3, and V4 segments, while set B is assembled with H5, V6, H7, and V8 segments. If set A generates right (left) circular polarization, set B generates left (right) circular polarization. The rotation angle θ of the linearly polarized light could then be controlled by changing the phase difference between the left and right circular polarizations with PS #4. As a demonstration of NEXAFS using this new polarization control, experiments were performed in the ultrahigh vacuum chamber of the SPring-8 BL07LSU. Hexagonal boron nitride (h-BN) films were prepared as samples. h-BN microcrystals have a flat shape, and the films were found to be oriented in two dimensions when mechanically pressurized. NEXAFS spectra were recorded by total electron yield at room temperature.

Figure 2(a) shows a collection of N K-edge NEXAFS spectra of oriented h-BN films, measured at the incident angle of 80° with linearly polarized light in the horizontal and vertical direction. The horizontal direction and the rotation axis of the sample were set perpendicular to each other. As shown in the figure, two prominent peaks were found at $h\nu = 401.5$ and 408.0 eV corresponding to π^* and σ^* orbitals of h-BN. In the horizontal polarization experiment, the intensity of the π^* peak is found to be larger while the σ^* peak is enhanced by vertical polarization. This spectral behavior is explained in terms of a dipole

transition in optical absorption. Since the π^* (σ^*) orbitals are oriented out-of-plane (in-plane), the peak intensity is enhanced when the linearly polarized light is parallel to the out-of-plane (in-plane) direction.

We focus on the π^* and σ^* peaks and track their intensity changes with the angle of linear polarization θ [Fig. 2(b)] Since this NEXAFS technique differs from the conventional one, it is hereafter referred to as a rotational NEXAFS measurement. The intensity at $h\nu = 401.5$ eV (π^* , plotted in green) is maximum at $\theta = 0, \pi, 2\pi$ (horizontal) and minimum at $\theta = \pi/2, 3\pi/2$ (vertical) while at $h\nu = 408.0$ eV (σ^* , plotted in yellow) the opposite trend is seen. This result is consistent with the conventional NEXAFS results shown in Fig. 2(a). However, the rotational NEXAFS data contain angle-dependent data, which increases the reliability of the experiment and thus allows more precise determination of orbital configuration. In future, this technique could be combined with nano-focusing and/or fast polarization switching by electromagnetic PSs. This will allow quick and sensitive detection of NEXAFS signals from non-uniform functional materials and enhance the potential of NEXAFS in modern science.

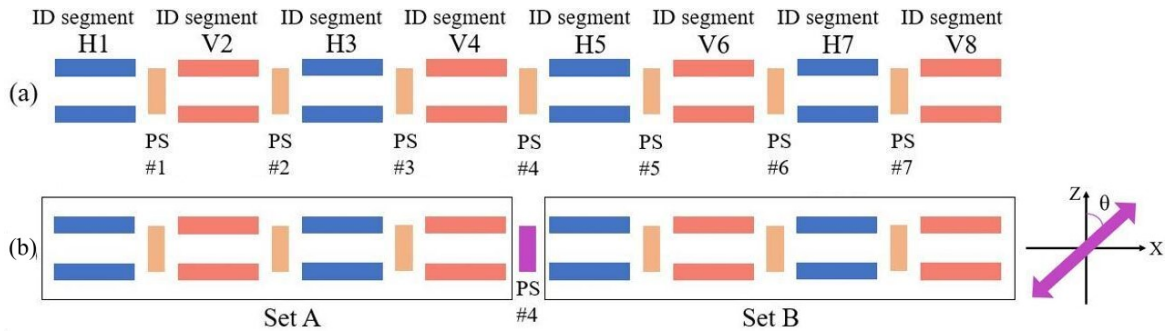


Fig. 1: Segmented cross undulator. (a) The light source composed of eight segments of the insertion device (ID) and seven phase shifters (PS's). Horizontal (H) and vertical (V) IDs are positioned alternately. (b) The setup for producing linear polarization at arbitrary azimuthal angles. Circularly polarized light with opposite helicities is produced by undulator sets A and B, and interfere with a relative phase difference controlled by PS #4.

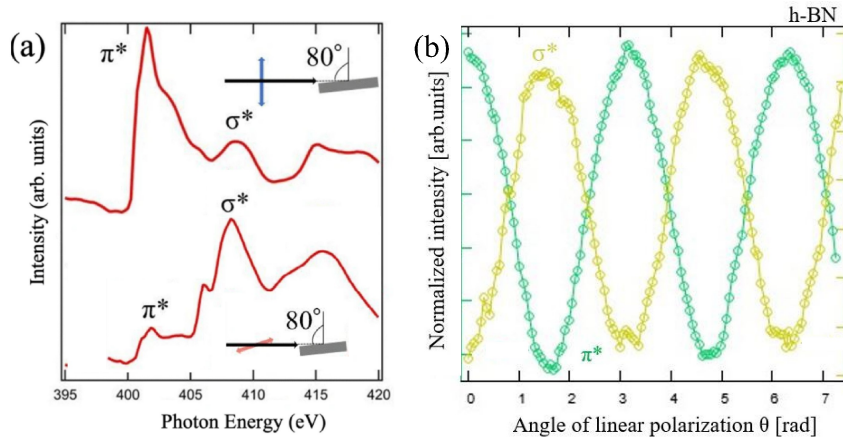


Fig. 2: NEXAFS spectra of h-BN recorded with a grazing incidence of 80° . (a) NEXAS measured by using the horizontal (top) and vertical (bottom) polarization. (a) Absorption intensity of the selected transition as indicated, plotted versus linear-polarization angle.

REFERENCES

- [1] J. Stöhr, NEXAFS Spectroscopy (Springer, Berlin, Heidelberg, 1992).
- [2] S. Yamamoto *et al.*, J. Synchrotron Rad. **21**, 352 (2014).

Coherence Effect of Intermediate State in Resonant Inelastic Soft X-ray Diffraction

J. Miyawaki^{1,3}, T. Yachi², S. Maki², K. Kanie² and Y. Harada³

¹*Institute for Advanced Synchrotron Light Source,
National Institutes for Quantum and Radiological Science and Technology*

²*Institute of Multidisciplinary Research for Advanced Materials, Tohoku University*

³*Institute for Solid State Physics, The University of Tokyo*

The fundamental determinants of the physical properties of materials (external field response) are elementary excitations such as phonons, magnons, and crystal field excitations. These elementary excitations are very sensitive to structural changes in materials, suggesting the importance to identify both the structure and these excitations simultaneously. Resonant inelastic X-ray scattering (RIXS) is the most direct method to observe these elementary excitations. Since elastic scattering contains information related to diffraction, RIXS also contains diffraction-derived structural information. Therefore, RIXS originally has the potential to correlate the structural information with the electronic state, i.e., to observe the electronic state in a structure-selective manner.

We have been conducting angle-resolved RIXS experiments with several Fe-containing nanoparticles to demonstrate the diffraction-assisted enhancement of the RIXS intensity using small angle X-ray scattering (SAXS), which is caused by diffraction phenomena from nanoparticles. The combined method of RIXS and SAXS is the inelastic version of SAXS and can be called small angle inelastic X-ray scattering (SAIXS). SAXS and SAIXS were measured at the Fe *L*-edge for two types of nanoparticles, Fe₃O₄ (insulator) and FePt (metal), and the angle dependence of the elastic scattering was clearly observed for both types of nanoparticles: SAXS in the soft X-ray region was successfully observed. On the other hand, we have reported that SAIXS was observed in FePt, but not in Fe₃O₄; the observation of SAIXS in FePt demonstrated that diffraction-assisted inelastic scattering can be realized when the conditions are met, but the results that SAIXS was not observed in Fe₃O₄ nanoparticle were not fully interpreted.

In order for angular (momentum) dependence of RIXS to be observed, the absorption and core-hole decay processes must be undisturbed by other relaxation effects such as electron-electron and electron-phonon interactions, and temporally coherent so that they can be regarded as RIXS processes. In addition, for the core-hole of the final state to be momentum-dependent, it must be delocalized so that it has well-defined crystal momentum in the crystal. This corresponds to spatial coherence, and both temporal and spatial coherence are considered to be necessary for SAIXS to be observed [1]. In this study, SAIXS was measured at near the threshold of the absorption edge, where the temporal coherence was enhanced [2], and the effects of temporal and spatial coherence were investigated.

Fig. 1(a) shows the SAXS results of Fe₃O₄ nanoparticles. The average particle size of the nanoparticles was 5.9 nm, and the incident energy was set to 707.5 eV, which was the threshold of the *L*₃ absorption edge. Linear vertical polarization was used to focus on the intensity of the elastic scattering. The SAXS profile obtained was slightly ambiguous than when measured at the top of the *L*₃ peak because of the weak resonance effect at the threshold of the absorption edge, but the similar SAXS profile were obtained. The profile was good agreement with the simulation, suggesting that the SAXS profiles were successfully observed. Next, RIXS measurements were performed at the same diffraction condition as SAXS, using linear horizontal polarization to focus on inelastic scattering. The SAIXS profile which was obtained by integrating the intensity of the inelastic component in RIXS spectra from ~1 to

~ 8 eV is shown in Fig. 1(b) together with the SAXS profile. No clear SAIXS profile was observed at the threshold of XAS, as was the case for measurements at the L_3 peak top.

Since the incident energy in this experiment was set at the threshold of the absorption edge, we believe that temporal coherence is $>50\%$, which is sufficiently high to observe SAIXS. Therefore, it is difficult to conclude that SAIXS was not observed due to the influence of temporal coherence. On the other hand, as for spatial coherence, since Fe_3O_4 is the insulator and valence orbitals are well localized, the observed inelastic components such as dd and charge-transfer excitations are mainly due to relaxation from the localized orbitals. Thus, the lack of SAIXS observed in Fe_3O_4 nanoparticles would be attributed to the lack of spatial coherence rather than temporal coherence. These results are consistent with the results of SAIXS observed for the metal FePt, in which the valence state is well delocalized in the crystal and the spatial coherence is high enough for SAIXS.

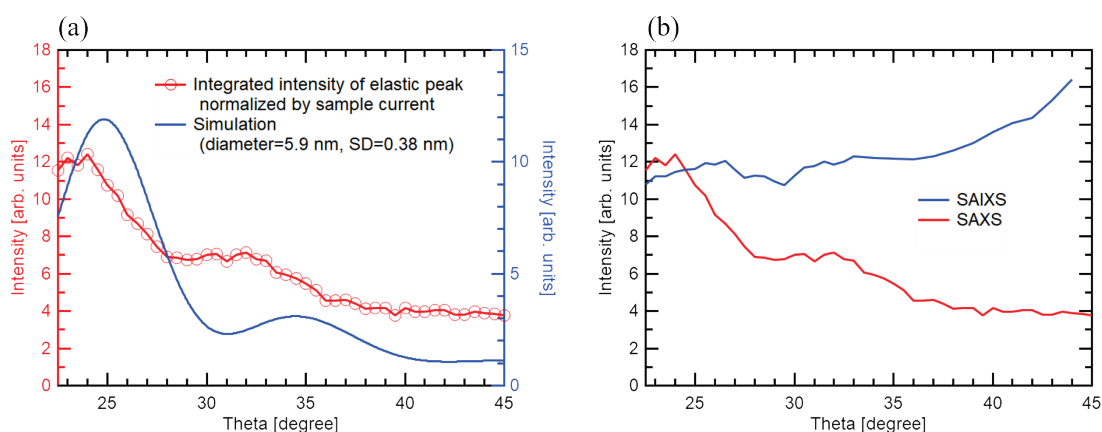


Fig. 1 SAXS and SAIXS of Fe_3O_4 nanoparticle measured at $h\nu=707.5$ eV. (a) Experimental (red) and simulated (blue) SAXS profile measured by σ polarization. (b) SAIXS spectra (blue) measured by π polarization compared with SAXS profile (red).

REFERENCES

- [1] Y. Ma, Phys. Rev. B **49**, 5799 (1994).
- [2] L. Zhang *et al.*, Fuller. Nanotub. Carbon Nanostructures **23**, 471 (2014).

ANALYSIS OF ELECTRONIC STATES OF PARTICULATE PHOTOCATALYSTS BY 3D NANO-ESCA

Takashi HISATOMI,^{1,2} Naoka NAGAMURA,^{2,3,4} Wenxiong ZHANG,⁵ Kenta OHISHI,^{2,3,4} Asako YOSHINARI,^{3,4} Shingo TAKEZAWA,^{3,4} Masaharu OSHIMA,⁵ Yoshihisa HARADA⁵

¹Research Initiative for Supra-Materials, Shinshu University

²Precursory Research for Embryonic Science and Technology, Japan Science and Technology Agency

³Research Center for Advanced Measurement and Characterization National Institute for Materials Science

⁴Department of Materials Science and Technology, Tokyo University of Science

⁵The Institute for Solid State Physics, The University of Tokyo

The water splitting reaction using particulate semiconductor photocatalysts is studied as a means of renewable solar hydrogen production on a large scale. BaTaO₂N is an oxynitride photocatalyst material having a band gap energy of 1.9 eV and band edge potentials suitable for both hydrogen and oxygen evolution from water [1,2]. The photocatalytic activity of this material is dependent strongly on the preparation methods. In many cases, the activity for the hydrogen evolution reaction utilizing excited electrons is low. This is probably because BaTaO₂N is an n-type semiconductor and has a large Schottky-type barrier that prevents the transfer of excited electrons at the interface with cocatalyst nanoparticles serving as an active site. In fact, it is known that doping Al³⁺ into the Ti⁴⁺ site of the SrTiO₃ photocatalyst to cancel the n-type semiconducting properties drastically improves the photocatalytic water splitting activity [3]. These facts suggest that there is a certain correlation between the semiconducting characters such as the Fermi level and the hydrogen evolution activity of semiconductor photocatalysts.

In this work, the electronic states of BaTaO₂N and SrTiO₃ photocatalysts were analysed by three-dimensional nano-electron spectroscopy for chemical analysis (3D-nano ESCA). With high spatial resolution reaching less than 100 nm, it is expected that the valence band spectrum of individual photocatalyst particles without signals originating from the conductive sample stage can be obtained [4]. This will allow us to determine the Fermi level of particulate photocatalyst materials and to investigate the correlation between the Fermi level and photocatalytic activity.

Two kinds of BaTaO₂N and SrTiO₃ were prepared according to literature. BaTaO₂N nitrided from BaCO₃ and Ta₂O₅ in the presence of RbCl flux, denoted as BaTaO₂N (RbCl), showed high hydrogen evolution activity [1]. The other BaTaO₂N nitrided from nominally Na_{1/4}Ba_{3/4}Zn_{1/4}Ta_{3/4}O₃ and BaCO₃ in the presence of NaCl flux, denoted as BaTaO₂N (NBZTO), showed high oxygen evolution activity [2]. Commercial SrTiO₃ as received, denoted as SrTiO₃, was hardly active in overall water splitting, while SrTiO₃ doped with Al in the presence of SrCl₂ flux, denoted as SrTiO₃:Al, was highly active in overall water splitting and showed an external quantum efficiency exceeding 90% in the near ultraviolet region [3]. These particulate photocatalysts had particle sizes of 200–500 nm and were immobilized on Au thin film by using the particle transfer method [5]. Figure 1 shows a scanning electron microscope image of a representative BaTaO₂N sample embedded on Au film.

The core level and valence band X-ray photoelectron spectroscopy (XPS) data were acquired using the 3D-nanoESCA at BL07LSU of SPring-8. The incident

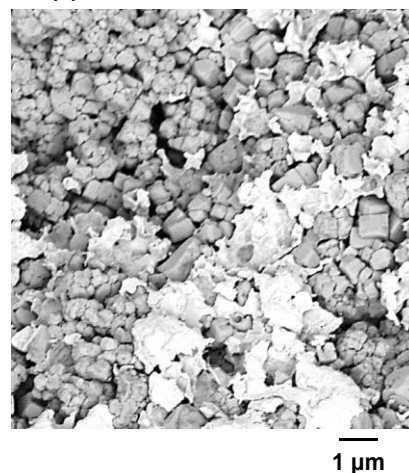


Figure 1. A scanning electron microscope image of BaTaO₂N (NBZTO) embedded on Au film.

photon energy was set to 1200 eV. The spectral data were acquired with energy and spatial resolutions of 100 meV and 200 nm, respectively.

It was possible to acquire a valence band spectrum of a particulate photocatalyst free from the signal of the underlying Au thin film by choosing the measurement spot carefully (Figure 2Ab). However, at almost all measurement points, the signal of Au 5d orbitals derived from Au fragments exposed from the gap among photocatalyst particles overlapped in the valence band region (Figure 2Aa), and spectra that could be used for the determination of the Fermi level was not obtained in a reasonable time. Therefore, the Fermi level shift was estimated from the change in the binding energy of core levels.

Figures 2B and 2C show Ta 4f and Ba 3d spectra of the BaTaO₂N materials, respectively. BaTaO₂N (RbCl) had binding energies smaller than BaTaO₂N (NBZTO) by 0.2 eV. The binding energy reflects the energy gap between the Fermi level and the core level. Given that the binding energy shift was attributable solely to the Fermi level shift, BaTaO₂N (RbCl) should have a Fermi level at a 0.2 eV more positive potential than BaTaO₂N (NBZTO). As a result, BaTaO₂N (RbCl) was closer to the intrinsic semiconductor and had a weaker Schottky-type barrier at the interface with the cocatalyst. This may account for the higher hydrogen evolution activity of BaTaO₂N (RbCl). However, the energy shift was relatively small. More comprehensive analysis of the materials properties will be needed to make a decisive conclusion. On the other hand, SrTiO₃:Al had binding energies smaller than SrTiO₃ by 0.4 eV for both Sr 3d and Ti 2p orbitals and thus was closer to the intrinsic semiconductor. This clear Fermi level shift confirms the correlation of the semiconducting properties and water splitting activity of the SrTiO₃ photocatalyst.

In summary, the Fermi level shift could be estimated from the core level shifts, although measurement results that took advantage of the high spatial resolution were not obtained. Considering that the observed signal is given by the weighted average of the signals from the particulate sample and Au, it may be possible to extract the signal of the sample by statistical analysis of a large number of spectra.

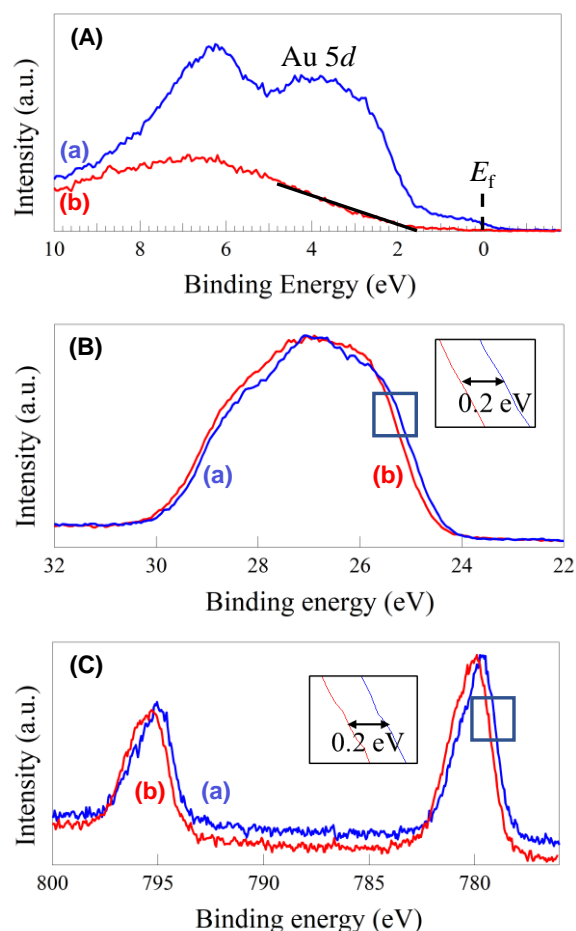


Figure 2. (A) Valence band, (B) Ta 4f, and (C) Ba 3d spectra of (a) BaTaO₂N (RbCl) and (b) BaTaO₂N (NBZTO). The valence band spectrum of BaTaO₂N (RbCl) was overwhelmed by the signal from Au fragments.

REFERENCES

- [1] Wang *et al.* *Nat. Commun.* **2021**, *12*, 1005.
- [2] Jadhav *et al.* *J. Mater. Chem. A* **2020**, *8*, 1127.
- [3] Takata *et al.* *Nature* **2020**, *581*, 411.
- [4] Sakai *et al.*, *Nanoscale* **2016**, *8*, 18893.
- [5] Minegishi *et al.* *Chem. Sci.* **2013**, *4*, 1120.

SPECTRAL IMAGING ANALYSIS OF EDGE-CONTROLLED 2D MATERIALS

Naoka NAGAMURA^{1,2,3}, Mitsuhiro OKADA⁴, Ryo NOUCHI^{3,5}, Tarojiro MATSUMURA⁴, Yasunobu ANDO⁴, Asako YOSHINARI^{1,2}, Shingo TAKEZAWA^{1,2}, Kenta OHISHI^{1,2,3}, Kentaro FUKU⁶, Wenxiong ZHANG⁷, and Masaharu OSHIMA⁷

¹National Institute for Materials Science (NIMS), Tsukuba, Ibaraki, Japan.

²Tokyo University of Science, Katsushika, Tokyo, Japan

³PRESTO, Japan Science and Technology Agency, Honcho, Saitama, Japan.

⁴National Institute of Advanced Industrial Science and Technology (AIST), Tsukuba, Ibaraki, Japan

⁵Osaka Metropolitan University, Sakai, Osaka, Japan

⁶Tohoku University, Sendai, Miyagi, Japan

⁷The University of Tokyo, Kashiwa, Chiba, Japan

In atomic layer semiconductor sheets, edge states are remarkably effective to the transport properties. Highly reactive dangling bonds exist at the edges of finite-size two-dimensional (2D) materials. Structures and chemical bonding states of the edges are easily modulated, so direct observation of edge states is important to discuss the characteristics of 2D materials. Here we have investigated the spatial distribution of electronic states and chemical bonding states of the edge-controlled functional 2D materials, the monolayer MoS₂-Nb-doped MoS₂ lateral homojunctions and the gate-controlled UV photo-oxidized graphene field effect transistors, using the 3D nano-ESCA[1] system at BL07LSU of SPring-8.

1. MoS₂-Nb-doped MoS₂ lateral homojunctions

Monolayer transition metal dichalcogenides (TMDs) are promising materials for various next-generation semiconductor devices. However, carrier doping techniques for TMDs have not been completely established yet. We synthesized monolayer MoS₂-Nb-doped MoS₂ lateral homojunctions using chemical vapor deposition (CVD).

To analyse the spatial elemental composition and the carrier distribution of MoS₂-MoS₂:Nb, we performed 3D nano-ESCA measurements. Peak fitting of X-ray photoemission spectroscopy (XPS) spectra was performed using the spectrum- adapted expectation-conditional maximization (ECM) algorithm[2,3].

The Mo 3*d* and S 2*s* core levels of the MoS₂:Nb region had smaller binding energies than those of the pure MoS₂ region ($\Delta \sim 0.3$ eV) as shown in Fig. 1(a). This difference was attributed to the Fermi-level (E_F) downshift by hole doping[4]. Fig. 1(b) presents the intensity mapping of Nb⁴⁺ 3*d*_{5/2} core level peak in a MoS₂-MoS₂:Nb sheet. Signals from Nb⁴⁺ were observed only in the edge regions. Moreover, in the peak position mapping of Mo⁴⁺ 3*d*_{5/2} (Fig. 1(c)), low-binding energy shift were observed also only at the edge region. Therefore, the grown MoS₂-MoS₂:Nb is revealed to have a built-in *p-n* lateral homojunction[5].

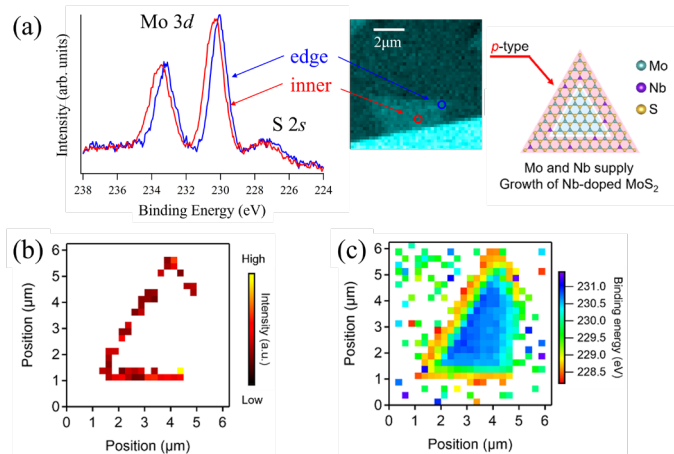


Figure 1 (a) Mo 3*d* and S 2*s* core level spectra measured at points indicated in the inserted image. Right picture is MoS₂-MoS₂:Nb growth strategy. (b) peak intensity mapping image of Nb⁴⁺ 3*d*_{5/2} and (c) peak position mapping image of Mo⁴⁺ 3*d*_{5/2} measured on MoS₂-MoS₂:Nb sheet.

2. Gate-controlled UV photo-oxidized graphene field effect transistor

Photo-oxidation is one of the means for surface modifications to control the electronic and chemical properties. Recently, the gate controllability of photo-oxidation reaction in graphene has been verified using a field-effect-transistor (FET) configuration[6,7]. However, the chemical structure of photo-oxidized graphene surface has not yet been experimentally measured. Then we performed an XPS analysis with a high spatial resolution using the 3D nano-ESCA.

Fig. 2(a) shows pin-point XPS spectra of C 1s taken at the edge region and the center region of the photo-oxidized graphene FET. The binding energy of the main peak at the edge is 0.12 eV lower than that at the center. This energy shift is considered to be caused by the Fermi-level (E_F) shift induced by charge doping[4]. The concentration of the doped holes in graphene at the edge is estimated to be $1.1 \times 10^{12} \text{ cm}^{-2}$, which is consistent with the previous studies on thermal annealing[8].

As oxidation reactions progress, the shape of the spectrum changes. Fig. 2(b) shows pin-point XPS spectra of C 1s at several locations in the heavily photo-oxidized graphene FET. Peak components at higher binding energies, derived from sp^3 bonding and carbon-oxygen chemical bonding, seems to increase as oxidation progresses.

Therefore, we revealed that the gate-controlled UV photo-oxidation reaction proceed as follows: hole doping via adsorbed molecules at the edge region \rightarrow defect introduction by chemical reactions with adsorbed molecules \rightarrow decomposition and disappearance[9].

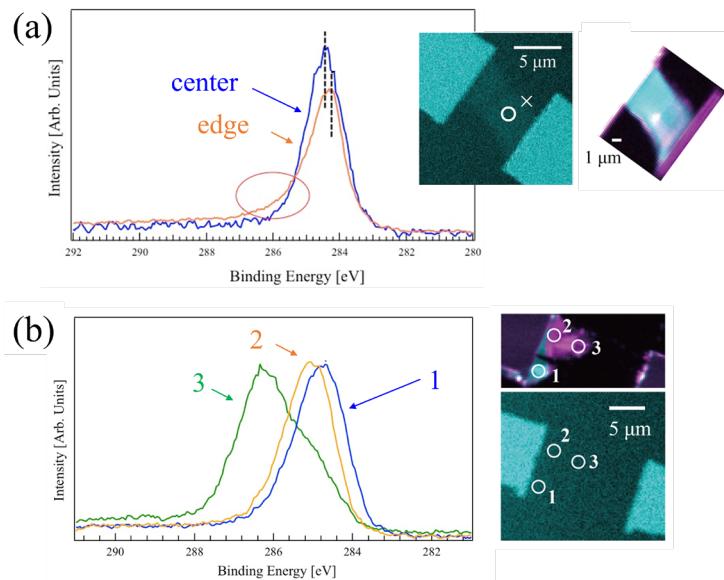


Figure 2 Pin-point C 1s and core level spectra measured at (a) the mildly photo-oxidized graphene FET and (b) the heavily photo-oxidized graphene FET.

REFERENCES

- [1] K. Horiba, Y. Nakamura, N. Nagamura, S. Toyoda, H. Kumigashira, M. Oshima, K. Amemiya, Y. Senba, and H. Ohashi, *Rev. Sci. Instrum.* **82**, 113701 (2011).
- [2] T. Matsumura, N. Nagamura, S. Akaho, K. Nagata, and Y. Ando, *Sci. Technol. Adv. Mater.* **20**, 733 (2019).
- [3] T. Matsumura, N. Nagamura, S. Akaho, K. Nagata, and Y. Ando, *Sci. Technol. Adv. Mater.: Methods* **1**, 45 (2021).
- [4] N. Nagamura, H. Fukidome, K. Nagashio, K. Horiba, T. Ide, K. Funakubo, K. Tashima, A. Toriumi, M. Suemitsu, K. Horn, and M. Oshima, *Carbon* **152**, 680 (2019).
- [5] M. Okada, N. Nagamura, T. Matsumura, Y. Ando, A. Lu, N. Okada, W. Chang, T. Nakanishi, T. Shimizu, T. Kubo, T. Irisawa, and T. Yamada, *APL Mater.* **9**, 121115 (2021).
- [6] N. Mitoma, and R. Nouchi, *Appl. Phys. Lett.* **103**, 201605 (2013).
- [7] R. Nouchi, M. Matsumoto, and N. Mitoma, *J. Mater. Chem. C* **7**, 1904 (2019).
- [8] S. Ryu, L. Liu, S. Berciaud, Y. Yu, H. Liu, P. Kim, G. W. Flynn, and L. E. Brus, *Nano Lett.* **10**, 4944 (2010).
- [9] N. Nagamura, S. Konno, M. Matsumoto, W. Zhang, M. Kotsugi, M. Oshima and R. Nouchi, *in preparation*.

RIXS-MCD Study of Chromium Trihalides CrX₃ (X = Cl, Br, I)

C. S. Pathiraja, J. N. Ranhili, Y. C. Shao, Y. -D. Chyang, B. Freelon

In the recently discovered 2D magnets formed by chromium trihalides CrX₃ (X = Cl, Br, I), a rich interplay between stacking and interlayer exchange has eventually led to a range of applications in spintronics, heterostructures, and twisted-layer devices. However, one of the most important open questions in this new field is what is the nature of the magnetic anisotropic interactions? Magnetic circular dichroism (MCD) in Resonant Inelastic X-ray Scattering (RIXS-MCD) is well-suited to address this issue because the technique allows the determination of d-orbitals that are associated with magnetic (dichroic) signals. The purpose of this beamtime was to use high-resolution RIXS-MCD and determine the detailed excitations that are relevant for the magnetic interaction in the CrX₃. Magnetic dichroic effect was studied for each d-d excitation to track their evolution.

During the beamtime, the data were taken for three samples CrCl₃, CrCl_{0.8}Br_{0.2} and CrI₃. Samples were aligned with the c- axis along antiparallel to the incident beam and the magnetic field was parallel to the incident beam. With the incident angle 45° at Room temperature, L-edge Cr RIXS-MCD were collected for both RCP and LCP at ~ 6 excitation energies with the incident wave vector directed along the direction of magnetization of the given 3 samples. Then the incident angle was changed to 90° and the measurements was repeated. Finally, the temperature was cooled down to liquid nitrogen temperature (~73.9K). At 74K, we could collect RIXS-MCD data only for CrCl₃ and CrCl_{0.8}Br_{0.2} because the limited time.

The experiment was successful, and we could observe some dichroism in the materials under given circumstances. In CrCl₃, the dichroism could be observed in the XAS, and it was almost vanished in the RIXS-MCD spectra (Figure 1). For the mix halide RIXS-MCD spectra, lots of the loss features had no noticeable dichroic dependence; however, there was some small circular polarization difference d-d region of 576.5 eV spectrum. Moreover, 3-5 eV loss region was rich with some features. Even though there was not much dichroic dependence in that region, the spectral evolution was interesting. (Figure 2) When comparing the XAS spectra for different materials, there was a shift in the peak position for CrI₃ nearly around 576.1 eV (Figure 3). As a summary, dichroism could observe in the XAS spectra and for the RIXS-MCD as we expected and further data analysis is still on the process. In the upcoming future, we are planning to work with theorists and obtain a theoretical point of view for our experimental results.

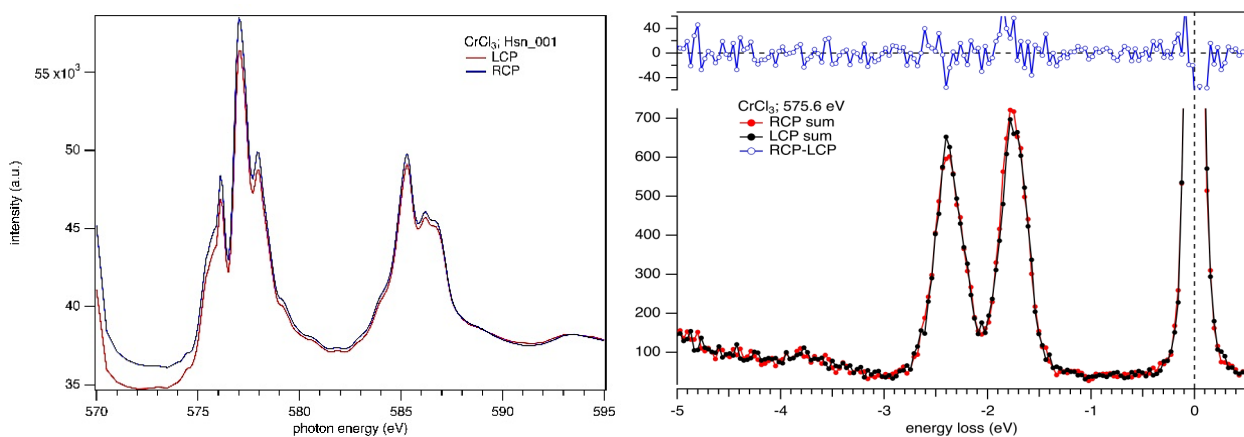


Figure 1: XAS and RIXS-MCD comparison of CrCl₃ for different excitation energies

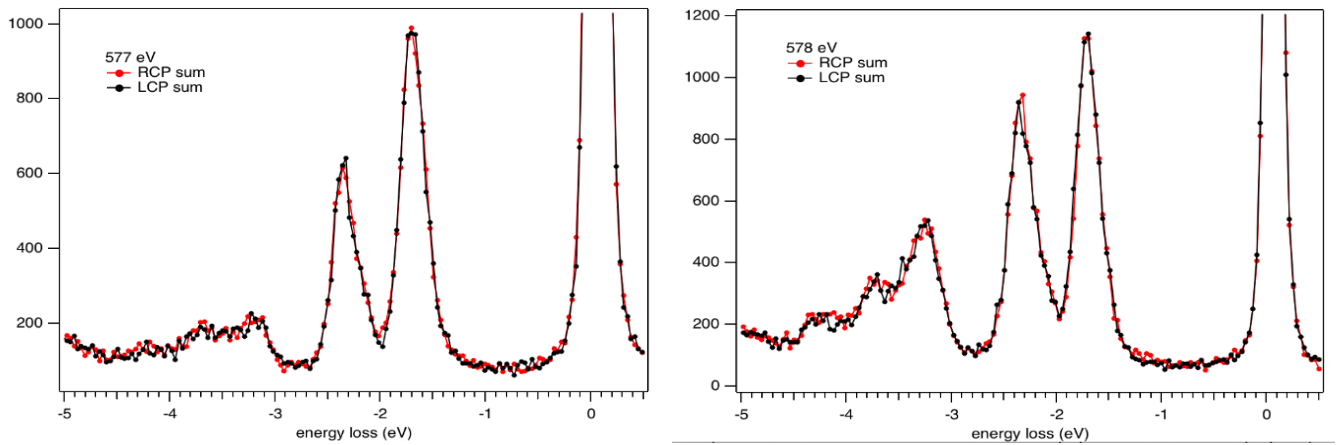


Figure 2: RIXS-MCD comparison of mix halide for different excitation energies

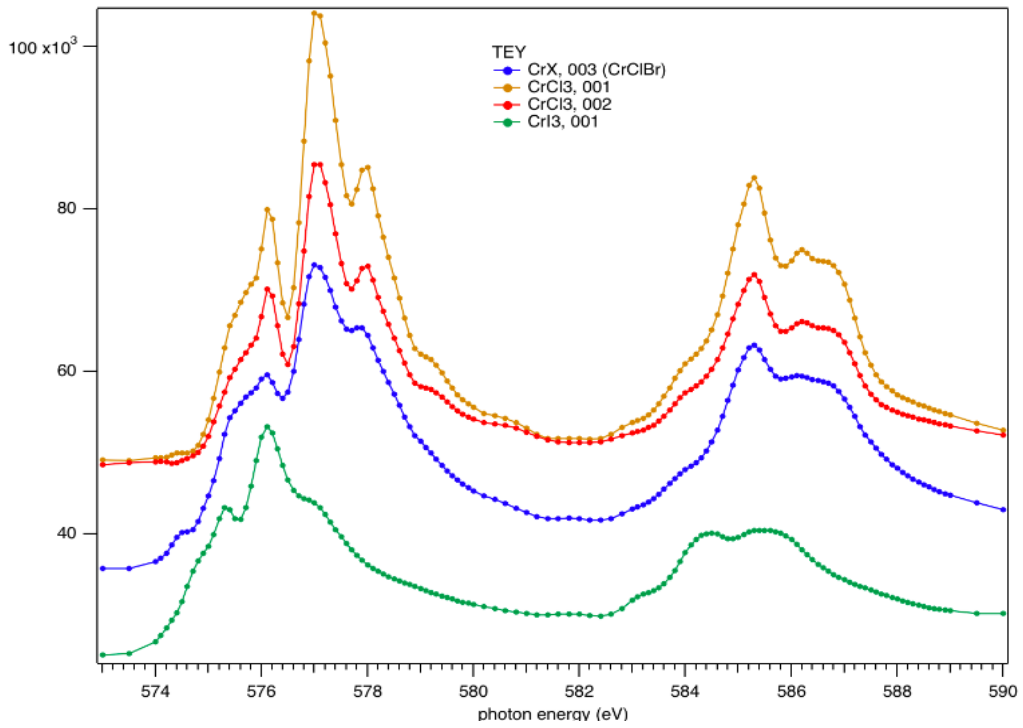


Figure 3: XAS comparison of different materials

INVESTIGATION OF ELECTRONIC STRUCTURE OF FE-CO SPINELS BY 2P3D RIXS AND L-EDGE XAS

Olaf Rüdiger,¹ Minmin Chen,¹ Derek Rice,¹ Hisao Kiuchi², Wenxiong Zhang², Ralph J. Ugalino³, Naoya Kurahashi², Yoshihisa Harada^{2,3}, Serena DeBeer¹

1. Max Planck Institute for Chemical Energy Conversion, Mülheim an der Ruhr, Germany

2. Synchrotron Radiation Laboratory, The Institute for Solid State Physics, The University of Tokyo

3. Graduate School of Frontier Sciences, The University of Tokyo

We collected cobalt L_{2,3} X-ray absorption spectra and 2p3d RIXS spectra of a series of Fe-loaded Co-based spinels relevant for water and alcohol oxidation reactions.^[1] Fe loading in a Co spinel is known to induce spinel inversion, but the degree of inversion cannot be easily obtained by XRD. Spinel has a general formula A²⁺B³⁺₂O₄, with A occupying a tetrahedral site (T_d) and B an octahedral one (O_h). For an inverse spinel, the +3 ions are equally

distributed among the T_d and O_h sites, while the +2 ion sits at a O_h site. In order to obtain the spectral signatures of the different sites, we collected spectra from the inverse spinel CoFe₂O₄, containing only Co²⁺_{oh}, and from the spinels CoAl₂O₄ (containing only Co²⁺_{Td}), and ZnCo₂O₄ (Co³⁺_{oh}).

Figure 1 shows the 2p3d RIXS spectra of Al₂CoO₄, Co₂ZnO₄, Co₃O₄, and CoFe₂O₄. The spectra show significant differences that can be assigned to the distinct spinel sites (Figure 1). At low incident energy we are primarily exciting the Co²⁺ ions, and we can clearly observe the differences between the T_d and O_h sites comparing the Al₂CoO₄ and CoFe₂O₄ samples, where the former has an emission signature at very low energy loss (0.5 eV). In contrast, the ZnCo₂O₄ sample has a transition at 0.7 eV, while the first inelastic peak for the inverse spinel appears at slightly higher energy.

To fully understand the different transitions, we are currently running multiplet calculations within the ORCA code.^[2] In Figure 2, we show preliminary calculations for the CoO and CoAl₂O₄ samples. The best fit to

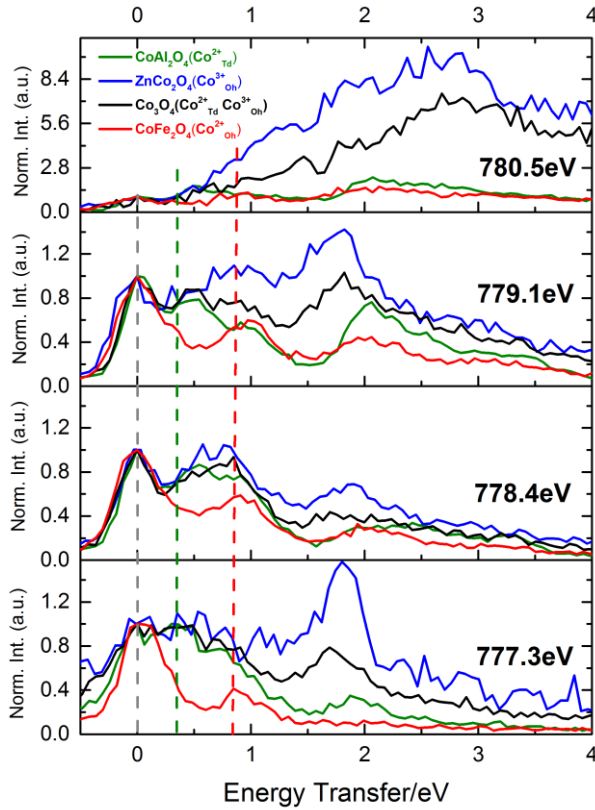


Figure 1. 2p3dRIXS of (a) CoAl₂O₄, (b) ZnCo₂O₄, (c) Co₃O₄, and (d) CoFe₂O₄ at incident energy 777.3eV, 778.4eV, 779.1eV, and 780.5eV respectively.

the spectra gave a 10 Dq value of 0.97 eV in a O_h geometry and a reduction of the atomic Slater-Condon parameters by 65% to account for covalency. For the T_d geometry we obtained a 10 Dq value of 0.52 eV and a reduction of the atomic Slater-Condon parameters of 70% for F_k and 63% for G_k have been used to reproduce CoAl₂O₄ spectra, although we found an inconsistency for the spectra at 779.1eV that we are still trying to refine. Similar calculations are being carried on for the Co³⁺_{oh} using the measured Co₂ZnO₄ as references.

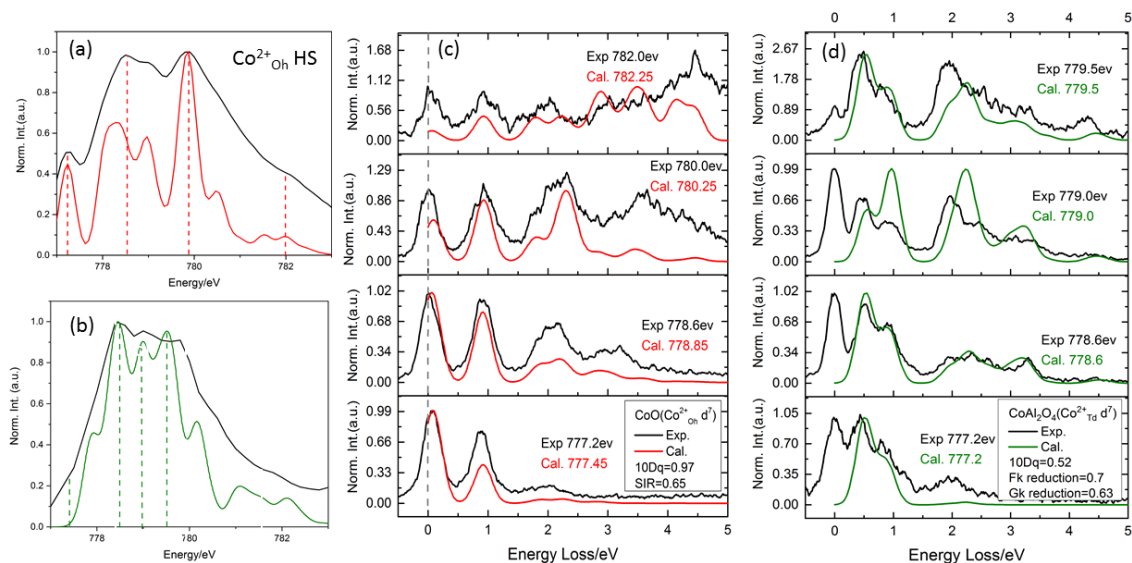


Figure 2. (a) L_3 -edge XAS calculation of $\text{Co}^{2+}_{\text{Oh}}$ and (b) $\text{Co}^{2+}_{\text{Td}}$ used the same parameter as their 2p3d RIXS calculation. (c) 2p3d RIXS calculation of $\text{Co}^{2+}_{\text{Oh}}$ and (d) $\text{Co}^{2+}_{\text{Td}}$ at incident energy 777.3eV, 778.4eV, 779.1eV, and 780.5eV with ORCA-LFT.

Figure 3 shows the 2p3d RIXS spectra of a series of Co-spinels with increasing amounts of Fe-loading at an incident excitation energy of 779.1 eV. The first conclusion that can be extracted is that the intensity at 0.5 eV, as well as the position of the peak between 0.6 and 1 eV energy transfer, appears to correlate with the degree of spinel inversion.

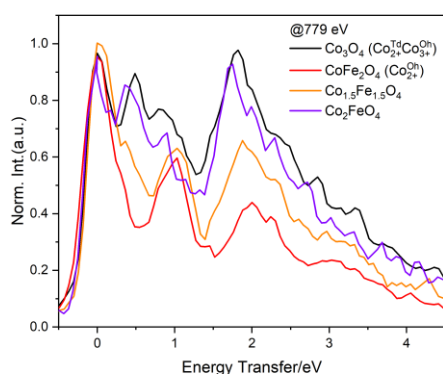


Figure 3. 2p3d RIXS spectra for a series of Fe-substituted Co spinels at 779.1 eV incident energy. The data has been smoothed by applying a 5-point moving average.

This way we can easily assign the Co_2FeO_4 as a spinel, while the $\text{Co}_{1.5}\text{Fe}_{1.5}\text{O}_4$ resembles much more the inverse spinel. Another interesting conclusion is that the position of the peaks for the Co_2FeO_4 is shifted with respect to the pure Co_3O_4 spinel. This is indicative of a modulation of the crystal field parameters of the Co ions by Fe substitution. Fe loading is known to improve the catalytic properties of Co spinel for water oxidation.^[1b] In the present work, we show evidence of how the Fe loading influences the Co electronic structure, as well as a technique to identify spinel inversion in these materials.

REFERENCES

- [1] a) D. Waffel, E. Budiyo, T. Porske, J. Bükler, T. Falk, Q. Fu, S. Schmidt, H. Tüysüz, M. Muhler, B. Peng, *Molecular Catalysis* **2020**, 498, 111251; b) E. Budiyo, M. Q. Yu, M. M. Chen, S. DeBeer, O. Rudiger, H. Tuysuz, *Acs Applied Energy Materials* **2020**, 3, 8583-8594.
- [2] F. Neese, *Wiley Interdisciplinary Reviews: Computational Molecular Science* **2012**, 2, 73-78.

STUDY ON THE ELECTRONIC STATE OF WATER MOLECULES IN POLYMER ELECTROLYTE MEMBRANES

Naoya Kurahashi¹, Ugalino Ralph John² and Yoshihisa Harada¹

¹*Synchrotron Radiation Laboratory, The Institute for Solid State Physics, The University of Tokyo*

²*Graduate School of Frontier Sciences, The University of Tokyo*

A fuel cell is a power generation device that directly converts chemical energy such as hydrogen into electrical energy. Fuel cells are highly energy efficient and do not generate carbon dioxide during power generation, so they are expected to contribute to the reduction of greenhouse gas emissions. In Japan, stationary fuel cells for home use were put on the market in 2009, and fuel cell vehicles were put on the market in 2014, but further spread and expansion are required. In particular, polymer electrolyte fuel cells (PEFCs) are being installed in automobiles because they are small and can generate electricity at low temperatures.

In PEFCs, when hydrogen gas is supplied to the anode, hydrogen ions (H^+) are generated on the electrodes. The generated hydrogen ions pass through the polymer electrolyte membrane (PEM) and move to the cathode, where hydrogen ions react with oxygen gas on the electrodes to generate energy and water molecules. Therefore, the polymer electrolyte membrane must have high gas barrier properties, water resistance, and mechanical strength, while allowing only hydrogen ions to permeate with high efficiency. Most of the polymers used in PEMs have a structure in which a strong acid group such as a sulfo group is introduced at the end of a hydrophobic skeleton. When these macromolecules aggregate, they take an inverted micelle structure and form nanometer-order channel structures¹. When the PEM is humidified, water is taken into the channel and hydrogen ions are released from the superacid group, which is thought to be a conduction path for hydrogen ions². Therefore, it is necessary to evaluate the hydrogen-bond property of water molecules in the PEM in order to understand the proton permeability. However, experimental research was lacking because it was difficult to directly observe the water molecules incorporated inside the membrane. The authors have previously attempted to evaluate the diffusion of water molecules incorporated into the Nafion membrane using nuclear magnetic resonance spectroscopy. As a result, it was clarified that the motility of water molecules changes significantly around a temperature of around 15 °C. The authors predicted that the cause of the change in motility was the change in the size of the proton channel, but we could not reach a conclusion only by NMR measurement. Therefore, we considered searching for the cause of the change in motility by investigating the electronic state of water molecules in the proton channel by soft X-ray emission spectroscopy. The sample was prepared by casting commercially available Nafion suspension onto a SiC plate and evaporate the solvent. By controlling both the temperature and humidity of the atmosphere control cell, the temperature dependence of the electronic state can be measured.

We evaluated the damage to Nafion because it was reported that soft X-rays would damage the fluorinated material. In the emission spectroscopy, the sample was moved at regular intervals to prevent damage to the SiC window and the sample, so that the same place is not continuously irradiated with synchrotron radiation. As a result of measuring the soft X-ray emission spectrum from Nafion by changing the X-ray irradiation time per point, it was concluded that damage to Nafion can be avoided if the X-ray irradiation is 5 seconds per point or less. Subsequently, the soft X-ray emission spectra from Nafion in a dry state with circulating nitrogen gas and in a humidified state at 80 % relative humidity were measured, and the difference spectrum between the two was calculated. As a result, only the emission spectrum derived from water molecules incorporated into the Nafion membrane could be extracted.

The soft X-ray emission spectra measured with photon energy of 550 eV and energy resolution of 150 meV is shown in Fig. 1. The spectra of water molecules confined in Nafion are quite different from that of bulk water measured under the same temperatures, with a largest peak that is thought to be $1b_1''$ at all temperatures. This suggests that water molecules confined in Nafion and in the bulk form different hydrogen bonding networks. On the other hand, since the emission spectrum has four overlapping peaks, it was difficult to evaluate the temperature dependence of the spectra. Therefore, in order to quantitatively evaluate the temperature dependence, we performed a peak-fitting of the emission spectrum with four Gaussians and evaluate the temperature dependence of the fitting parameters. Fitting of the spectra was performed using the following function,

$$I(x) = I_0 + \sum_i \frac{A_i}{\sqrt{2\pi\sigma_i^2}} e^{-\frac{(x-X_i)^2}{2\sigma_i^2}} \quad (i = 1b_2, 3a_1, 1b_1', 1b_1'') \quad (1)$$

where I_0 , A_i , X_i , and σ_i are the baseline, peak area, peak position, and standard deviation of the peak, respectively. As a result, the peak area of $1b_1'$ and $1b_1''$ show an interesting temperature dependence (Fig. 2). The $1b_1'$ emission intensity of water molecules confined into Nafion reached a maximum at 18 °C, while the $1b_1''$ emission intensity reached a minimum at 18 °C. The $1b_1'$ and $1b_1''$ intensities of bulk water showed monotonic changes in the range from 1 to 50 °C. This suggests that the water molecules confined into Nafion reach a maximum rate of

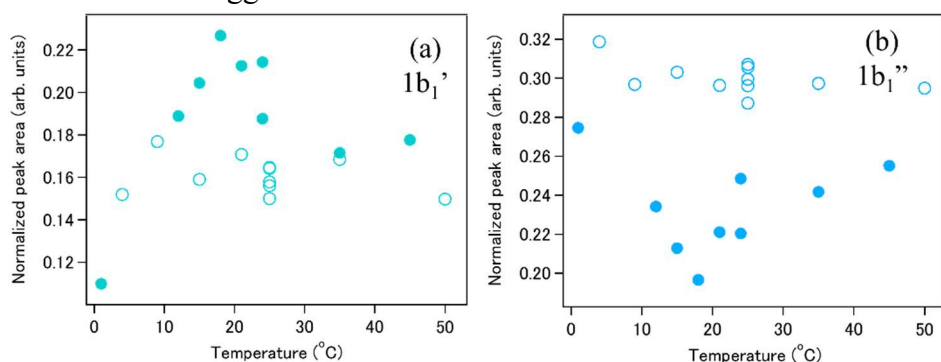


Fig. 2 Temperature dependence of $1b_1'$ (a) and $1b_1''$ (b) peak areas by fitting. Filled and open circles are the results for water in Nafion and for bulk water, respectively. The result of Nafion was that the area of $1b_1'$ was the largest and the area of $1b_1''$ was the smallest at 18 °C.

REFERENCES

- [1] M. Rikukawa, *Journal of Synthetic Organic Chemistry*, 66, 488 (2008).
- [2] M. Yoshida-Hirahara *et al.*, *RSC Adv.*, 10, 12810 (2020).

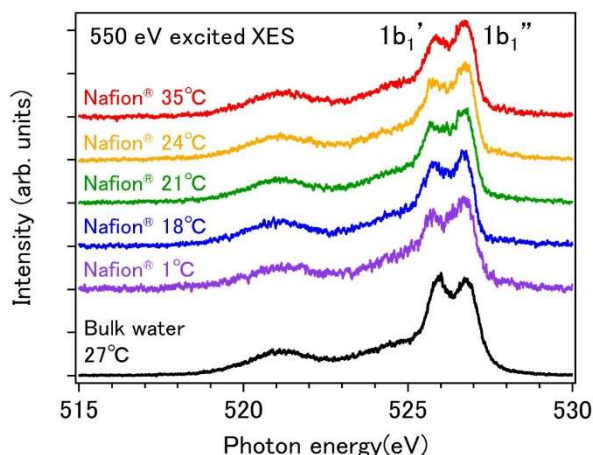


Fig. 1 Soft X-ray emission spectrum of bulk water and water molecules in Nafion at 80% relative humidity

hydrogen bonding in tetrahedral coordination around 18 °C. Combined with the results of previous NMR studies, this suggests that the size of proton channels in Nafion may change around 18 °C.

ELECTRONIC STATES OF FUNCTIONAL MATERIALS IN HYDROGEN ADSORPTION/DESORPTION STUDIED BY AMBIENT PRESSURE SOFT X-RAY PHOTOELECTRON SPECTROSCOPY

F. OZAKI, W. OSADA, Y. CHOI, H. YOSHIOKA, S. TANAKA, K. MUKAI, M. HORIO, I. MATSUDA and J. YOSHINOBU

The Institute for Solid State Physics, The University of Tokyo

Introduction

In this research, we have studied the electronic and chemical states of functional materials whose electronic and chemical properties are changed by the interaction with hydrogen, by the use of ambient-pressure photoelectron spectroscopy (AP-XPS) at BL07LSU, SPring-8. Molybdenum disulfide (MoS_2) is a layered material and it has been used as a hydrogenation catalyst [1]. For example, MoS_2 has long been used as a hydrodesulfurization catalyst to selectively remove sulfur from petroleum to produce clean fuels [2]. MoS_2 has also attracted attention for its high activity as a hydrogen evolution electrocatalyst [3]. Thus, understanding the interactions between MoS_2 surfaces and hydrogen is an important issue. Here, we report the interaction of the MoS_2 basal surface and the Pd-deposited MoS_2 basal surface with hydrogen, because it is known that the basal plane of MoS_2 is inert for the dissociation of molecular hydrogen at room temperature.

Experimental

A natural MoS_2 crystal was used as a sample. After the sample was mounted on metal plates, scotch tape was used to peel the surface layers off. The sample was transferred to a load lock chamber within 10 min after the exfoliation and annealed at approximately 550 K for 30 min in an ultrahigh vacuum (UHV) chamber. To prepare a Pd-deposited MoS_2 surface, Pd atoms were deposited on a MoS_2 basal surface at 300 K by resistive heating of a Pd wire. The deposited Pd atoms were considered to aggregate to form islands on the MoS_2 surface at 300 K [4].

AP-XPS measurements were performed in a chamber equipped with a hemispherical electron energy analyzer (SPECS, PHOIBOS150 NAP) at BL07LSU of SPring-8, Japan [5]. All XPS spectra were obtained at room temperature using the photon energy of 680 eV. The binding energies of the measured spectra were calibrated by the Fermi energy of a gold foil on the sample holder. The high-purity H_2 gas was introduced into an ambient-pressure gas cell, where the base pressure was below 5×10^{-10} mbar.

Results and discussion

In the Mo 3d, S 2p, and valence-band photoelectron spectra of a bare MoS_2 surface, little change was observed in the energy shift before and after exposure to hydrogen gas (not shown here; please refer to Ref. 6). At the Pd-deposited MoS_2 surface under hydrogen gas exposure, the Mo 3d, S 2p, valence-band and Pd 3d XPS spectra were measured by AP-XPS [Figure 1(a)–(d)]. The peak energy of Pd 3d gradually shifted to a higher binding energy as a function of hydrogen exposure, which can be ascribed to the dissociative adsorption of molecular hydrogen. We performed fitting of the Pd 3d_{5/2} XPS spectra before and after the exposure to hydrogen gas. The fitting result before hydrogen exposure is shown in the lower part of Fig. 1(e), where the low energy component (334.9 eV, green) and high energy component (335.6 eV, blue) can be assigned to the surface and bulk Pd components in the Pd island, respectively. Note that each peak in the photoelectron spectra (Mo 3d, S 2p, and valence-band) shifted to a lower binding energy with 0.1 eV [Figure 1(f)]. These results indicate that the dissociation of molecular hydrogen and the adsorption of atomic hydrogen occur on the Pd-deposited sites on the MoS_2 surface, and thereafter hydrogen atoms spillover onto the MoS_2 surface.

The present study shows that the active site for the dissociation of molecular hydrogen is created on an inert MoS₂ basal surface by Pd deposition. In addition, the electronic state of the MoS₂ substrate is modulated by hydrogen atoms spilled over onto the MoS₂ surface. The details of this study have been published elsewhere [6].

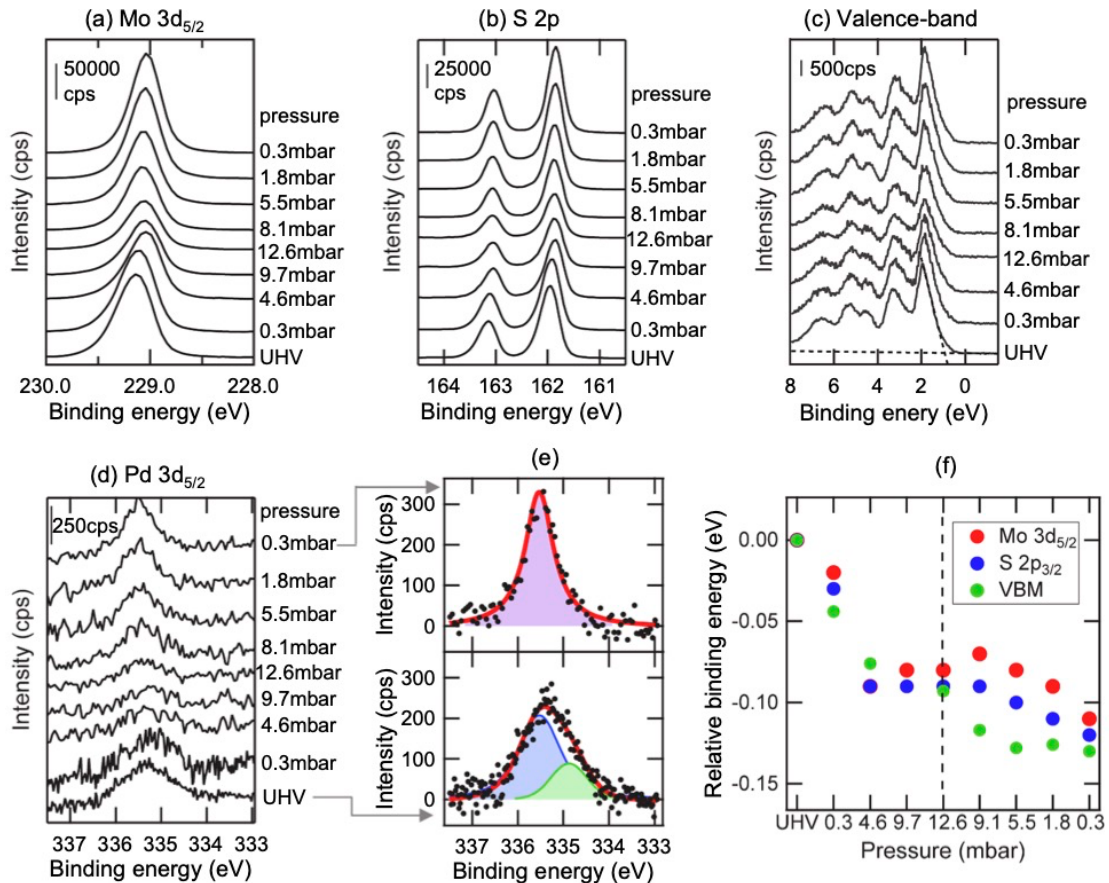


Figure 1 (a) Mo 3d_{5/2}, (b) S 2p, (c) valence-band, and (d) Pd 3d_{5/2} spectra of the Pd/MoS₂ as a function of H₂ gas pressure at 300 K. The amount of deposited Pd was estimated to be 2.0 % for the amount of Mo atoms on the outermost MoS₂ layer. (e) The upper and lower figures show the fitting results for the Pd 3d_{5/2} AP-XPS spectra before and after the hydrogen exposure, respectively. The green component and blue component in the lower figure are assigned to be surface and bulk components of the Pd islands, while the pink component consists of both the bulk component and hydrogen atoms-adsorbed surface component. (f) The relative binding energies for the Mo 3d_{5/2}, S 2p_{3/2} and valence band maximum (VBM) as a function gas exposure process. © 2022 Elsevier B.V [6].

ACKNOWLEDGMENTS

The AP-XPS measurements using synchrotron radiation were performed at SPring-8 BL07LSU as joint research in the Synchrotron Radiation Research Organization, The Institute for Solid State Physics, The University of Tokyo (Proposal No. 2020A7481, 2021A7426). We thank Mr. Yu Tsuchihara at the initial stage of this research.

REFERENCES

- [1] J. Mao et al., *Front. Phys.* **13** (2018) 138118.
- [2] H. Topsøe et al., *Ind. Eng. Chem. Fundamen.* **25** (1986) 25.
- [3] Y. Yan et al., *ACS Catal.* **4** (2014) 1693.
- [4] H. Dong et al., *ACS Appl. Mater. Interfaces* **9** (2017) 38977.
- [5] T. Koitaya et al., *Top. Catal.* **59** (2016) 526.
- [6] F. Ozaki et al., *Appl. Surf. Sci.* **593** (2022)153313.

O K-edge soft X-ray emission spectroscopy of the solvents in electrolyte solutions for redox flow batteries

Eiji Hosono^{1,2}, Daisuke Asakura^{2,3}, Akihiro Ohira³, Wenxiong Zhang⁴, Naoya Kurahashi⁴,
Ralph J. Ugalino⁴, Hisao Kiuchi⁴, and Yoshihisa Harada^{2,4}

¹*Global Zero Emission Research Center, National Institute of Advanced Industrial Science and Technology (AIST)*

²*AIST-UTokyo Advanced Operando-Measurement Technology Open Innovation Laboratory, AIST*

³*Research Institute for Energy Conservation, AIST*

⁴*Synchrotron Radiation Laboratory, The Institute for Solid State Physics, The University of Tokyo*

Redox flow battery (RFB) is a rechargeable battery which is attractive for application to large-scale energy storage system. RFBs consist of electrolyte solutions containing the active materials, positive and negative electrodes soaked in the electrolyte solutions, and an electrolyte membrane that separates the two electrodes. It is characteristic for RFBs that the electrolyte solutions are mainly responsible for the redox reactions unlike Li-ion batteries where the solid-state electrodes are redox active. For example, vanadium RFB is most promising for practical use. The redox reaction is vanadium's $V^{4+} \rightleftharpoons V^{5+}$ in the electrolyte for cathode and $V^{3+} \rightleftharpoons V^{2+}$ in that for anode. Thus, the battery capacity depends on the vanadium ion concentration in the electrolyte solutions.³

To increase the capacity of RFBs, it is important to understand the redox reaction at the interface between the active material and the electrode in the electrolyte solution, which is directly connected with the concentration. Thus, the electronic structure analysis is of particular importance. Especially, it is necessary to clarify the solvation and de-solvation behavior of the active material due to the redox reaction. X-ray emission spectroscopy (XES) is one of the promising techniques to understand those properties. For aqueous electrolyte solutions, O K-edge XES is highly useful to investigate the coordination mechanisms of H₂O molecules. In this study, we apply O K-edge XES to aqueous electrolyte solutions including organic active materials.¹

The O K-edge XES measurements were carried out by using HORNET spectrometer at BL07LSU, SPring-8. The energy resolution was set to 170 meV at 540 eV. The aqueous electrolyte solutions including organic active materials and reference solution samples were put in a flow-type liquid cell with a 150-nm-thick Si₃N₄ membrane window to separate the liquid samples from vacuum. The samples were flowed with a flow rate of 1 ml/min by a peristaltic pump (Fig. 1) during the XES measurements.

Figure 2 shows the O K-edge XES spectra for pure H₂O (25 °C) and 1 M NaCl/H₂O (room temperature) that is used as the solvent of the electrolyte solutions. The excitation energy was 550 eV in the post-edge region at the O K edge. The peaks around 521.2, 524.6, 525.8 and 527.7 eV are attributed to 1b₂, 3a₁, 1b₁' and 1b₁'' as reported in previous papers.^{2,3} The 1b₁' and 1b₁'' peaks are of ice-like tetrahedral coordination of H₂O molecules and distorted coordination environment, respectively. For 1 M NaCl/H₂O, the 1b₁' peak is slightly lower than the 1b₁'' peak in contrast to the spectrum for pure H₂O, suggesting that the H₂O molecules in 1 M NaCl/H₂O should be less coordinated than those in pure H₂O. Moreover, the higher 3a₁ peak, which is dipole-forbidden transition in tetrahedral symmetry, for 1 M NaCl/H₂O indicates that the H₂O tetrahedron is relatively distorted. The electrolyte solutions including organic active materials showed similar tendencies, while slight differences in the O K-edge XES spectra were observed among the solution samples. In the near future, the XES

spectra will be analyzed in detail. Then, we will try the *operando* XES with charge-discharge measurement.

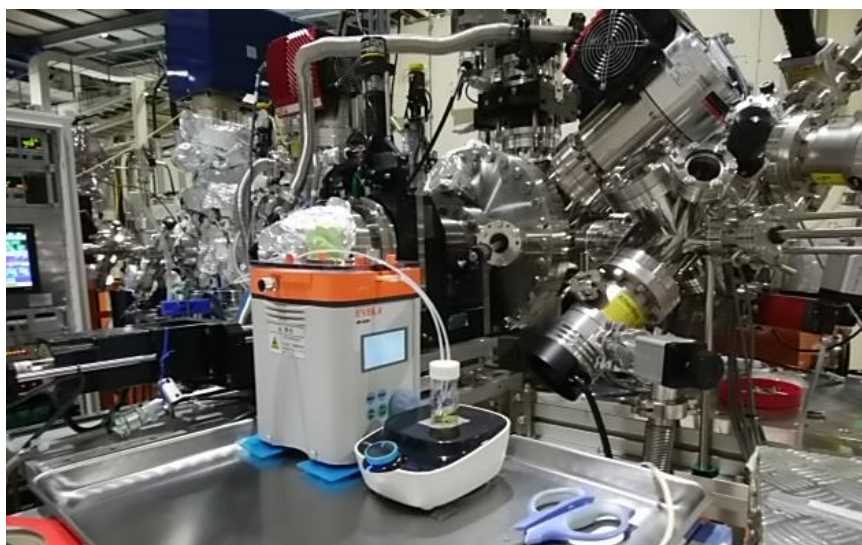


Fig. 1. A picture of the liquid flow system with a peristaltic pump for the *in situ* XES measurements.

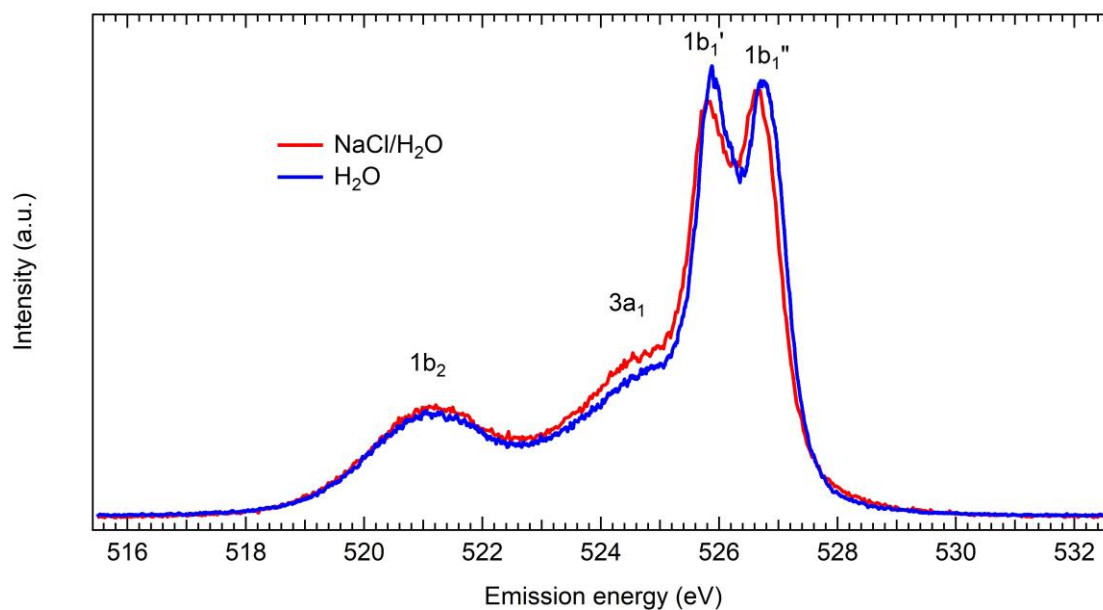


Fig. 2. O *K*-edge XES spectra for NaCl/H₂O and H₂O. The excitation energy was set to 550 eV.

REFERENCES

- [1] A. Ohira *et al.*, ACS Appl. Energy Mater. **3**, 4377 (2020).
- [2] T. Tokushima *et al.*, Chem. Phys. Lett. **460**, 387 (2008).
- [3] K. Yamazoe *et al.*, Langmuir **33**, 3954 (2017).

Co L_3 -edge Soft X-ray Emission spectroscopy of LiCoO_2 for Li-ion batteries

Daisuke Asakura^{1,2}, Eiji Hosono^{2,3}, Kosuke Yamazoe⁴, Naoya Kurahashi⁴, Ralph J. Ugalino⁴, Hisao Kiuchi⁴, and Yoshihisa Harada^{2,4}

¹*Research Institute for Energy Conservation, National Institute of Advanced Industrial Science and Technology (AIST)*

²*AIST-UTokyo Advanced Operando-Measurement Technology Open Innovation Laboratory, AIST*

³*Global Zero Emission Research Center, AIST*

⁴*Synchrotron Radiation Laboratory, The Institute for Solid State Physics, The University of Tokyo*

Li-ion battery (LIB) is one of the key energy-storage devices for CO_2 reduction. To further enhance the performances of LIBs for applications to electric vehicles and large-scale stationary energy storage systems, increasing the charge-discharge capacity of the cathode is highly demanded. Electronic-structure analysis using X-ray spectroscopy has been playing an important role on the clarification of the redox mechanism of cathode materials, which will lead to increase of the charge-discharge capacity. By clarifying the redox mechanism of typical cathode materials, strategies for designing novel cathode materials could be obtained.

We have been studying the electronic structure of several cathode materials using soft X-ray absorption (XAS) and emission spectroscopy (XES). For example, the Mn L -edge XAS and XES studies for LiMn_2O_4 revealed the redox reaction of $\text{Mn}^{3+} \leftrightarrow \text{Mn}^{4+}$ at the Mn^{3+} site in the initial state. The Mn^{4+} state has very strong charge-transfer effect between the O $2p$ and Mn $3d$ orbitals, resulting in the important role of O $2p$ orbital on the redox reaction.^{1,2} For LiFePO_4 , the redox reaction of Fe was confirmed by Fe L -edge XAS and XES, which was attributed to simple ionic redox of $\text{Fe}^{2+} \leftrightarrow \text{Fe}^{3+}$.³ Then, LiCoO_2 (LCO) is a prototypical cathode material for practical use like LiMn_2O_4 and LiFePO_4 . While the electronic structure of LCO has been studied by XAS,⁴ we demonstrate the Co L -edge XES to further understand the Co $3d$ and O $2p$ orbitals.

Powdered LCO sample was pasted with acetylene black and PTFE. The pasted LCO electrode was assembled as a three-electrode beaker cell with Li-metal counter and reference electrodes and an organic electrolyte solution. We prepared two cells to make charged-state and discharged-state samples with different modes by cyclic voltammetry. The charged/discharged cells were disassembled in an Ar-filled glovebox. The LCO samples were transferred from the glovebox to a transfer vessel without exposure to the air. *Ex situ* Co L -edge XAS and XES measurements for the pristine and the two charged samples were carried out by HORNET spectrometer at BL07LSU, SPring-8. The energy resolution for the XES measurement was set to 330 meV at 785 eV.

Figure 1 shows the Co L_3 -edge XES spectra measured with an excitation energy of 780.4 eV. Considering the Co $L_{3,2}$ -edge XAS results (not shown), the XES spectrum for the initial state should be of Co^{3+} low-spin state as with the XAS spectrum. On the other hand, the XES line shape is relatively different from that for LaCoO_3 having a Co^{3+} low-spin electron configuration.⁵ One of the reasons should be the lower symmetry of the CoO_6 octahedron in LCO, which should reflect the different structures for the dd excitation around 779 eV compared to the XES results for LaCoO_3 .⁵ These differences could be obtained by the high-resolution XES while the XAS line shapes of both LCO and LaCoO_3 are quite similar.

For the charged state, the XES line shape is greatly changed, indicating that the oxidation reaction of Co due to charge (Li-extraction) reaction. For the discharged state, the line shape is almost the same as the initial state. Therefore, the redox reaction of Co is highly reversible.

The XES spectra will be analyzed by using charge-transfer multiplet calculations in detail. We will focus on the charge-transfer effect between the O 2*p* and Co 3*d* orbitals like LiMn₂O₄.^{1,2} Then, the relation between the electronic structure and the electrode performance will be further investigated. Also, we will try the *operando* measurement with an all-solid-state-type *operando* cell for LIB (under construction), because LCO works in all-solid-state LIB⁶ which is highly attractive for application to electric vehicles.

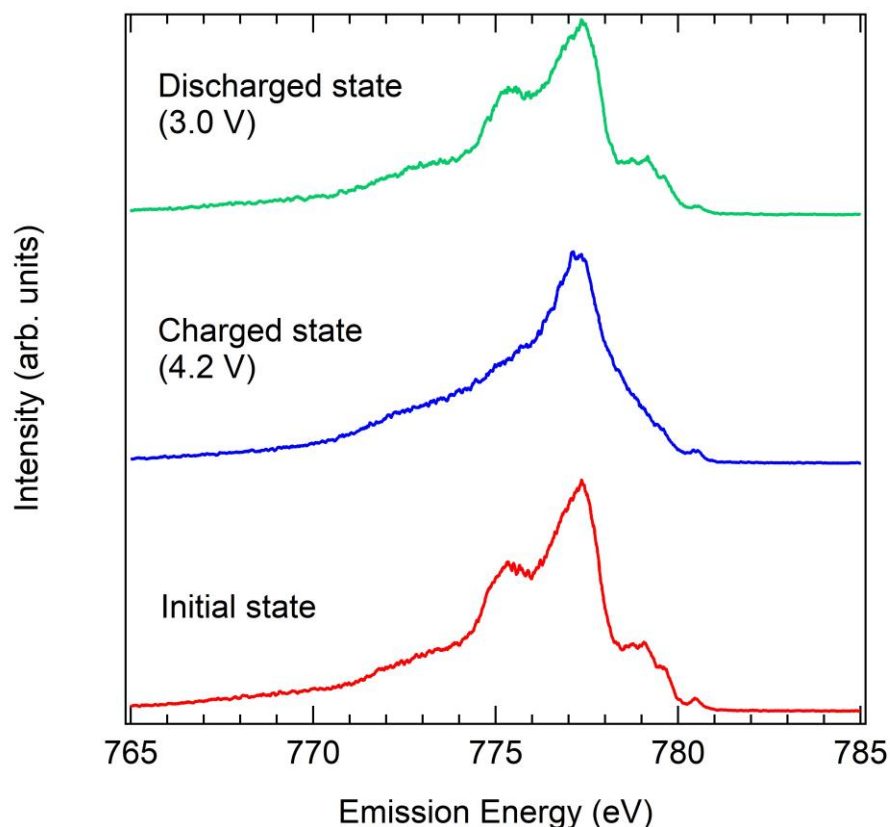


Fig. 1. Co *L*₃-edge XES spectra for LiCoO₂. The excitation energy was set to 780.4 eV.

REFERENCES

- [1] D. Asakura *et al.*, *Electrochem. Commun.* **50**, 93 (2015).
- [2] D. Asakura *et al.*, *Phys. Chem. Chem. Phys.* **21**, 18363 (2019).
- [3] D. Asakura *et al.*, *ChemPhysChem* **19**, 988 (2018).
- [4] For example, W.-S. Yoon *et al.*, *J. Phys. Chem. B* **106**, 2526 (2002) and T. Mizokawa *et al.*, *Phys. Rev. Lett.* **111**, 056404 (2013).
- [5] Y. Yokoyama *et al.*, *Phys. Rev. Lett.* **120**, 206402 (2018).
- [6] For example, Y. Kato *et al.*, *J. Phys. Chem. Lett.* **9**, 607 (2018).

REAL-TIME OBSERVATION OF HYDROGEN-ABSORPTION PROCESS IN Pd-Au ALLOYS BY OPERANDO AP-XPS

Takanori KOITAYA,^{1,2} Susumu YAMAMOTO,^{3,4} Masafumi HORIO,⁵ Iwao MATSUDA,⁵
Jun YOSHINOBU,⁵ and Toshihiko YOKOYAMA¹

1 Department of Materials Molecular Science, Institute for Molecular Science

2 Precursory Research for Embryonic Science and Technology (PRESTO), Japan Science and Technology Agency (JST)

3 International Center for Synchrotron Radiation Innovation Smart (SRIS), Tohoku University

4 Institute of Multidisciplinary Research for Advanced Materials (IMRAM), Tohoku University

5 The Institute for Solid State Physics, The University of Tokyo

Palladium-based alloys are widely known as hydrogen storage materials, and hydrogen absorption/desorption processes on the sample surfaces have been extensively studied. Palladium-gold (Pd-Au) alloy is expected to be used in various fields such as a hydrogen sensor [1] and a heterogeneous catalyst [2]. It has been also revealed that the adding gold to palladium promotes hydrogen absorption compared with pure palladium, which is caused by destabilization of chemisorbed surface hydrogen and decrease of a hydrogen penetration barrier from the surface into the subsurface [3].

In order to clarify the effects of the alloying with gold in the hydrogen absorption process, it is very important to perform operando spectroscopy under the conditions in which the absorption of hydrogen occurs. In this study, we measured the electronic states of the Pd-Au alloys during the hydrogen adsorption/desorption processes by soft X-ray near ambient-pressure photoelectron spectroscopy (AP-XPS), to reveal the nature of the interaction between the palladium alloy and absorbed hydrogen.

The experiments were performed using the AP-XPS system installed at the SPring-8 BL07LSU. Recently, the AP-XPS apparatus was improved, which enables AP-XPS measurements at higher gas-phase pressures up to 100 mbar. As a result, real-time AP-XPS measurements of the hydrogen adsorption/desorption processes have become possible with enough signal intensity and energy resolution to detect change in the chemical states of the Pd-Au alloys by the interaction with absorbed hydrogen. Before the AP-XPS experiments, the Pd-Au samples were cleaned by a cycle of Ar⁺ ion sputtering and annealing.

A series of AP-XPS spectra were measured while controlling the hydrogen pressure with a constant ramp rate ($\beta = 0.01$ mbar/s) at a sample temperature of 297.2 K. Figures 1(a) and (b) show the Pd 3d and Au 4f AP-XPS spectra of the Pd-Au alloy sample during the absorption and desorption processes as a function of hydrogen pressure. When the hydrogen pressure rises to about 15 mbar, hydrogen absorption occurs and the core-level peaks of the substrate change accordingly (Fig. 1(a)). In Fig. 1 (b), the spectral change in the hydrogen desorption process is observed at hydrogen pressure of 5 mbar. The transition pressure is clearly different between the absorption process and the desorption process (pressure hysteresis). This result indicates that the observed change in the chemical states of the alloy is caused by a metal-hydride phase transition.

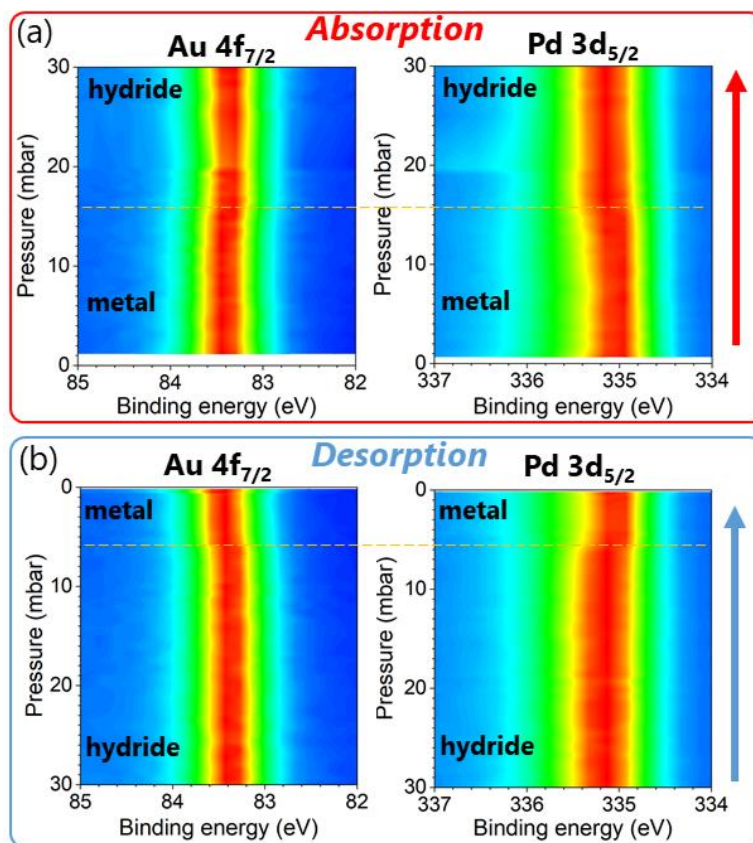


Figure 1. A series of Au 4f and Pd 3d AP-XPS spectra of the Pd-Au alloy (Au: 12 at%) in (a) absorption and (b) desorption processes as a function of hydrogen pressure. The gas-phase pressure was linearly changed at a constant rate of 0.01 mbar/s, whereas sample temperature was kept at 297.2 K. All the spectra were measured at photon energy of 1600 eV.

REFERENCES

- [1] C. Wadell et al., *Nano Lett.* **15**, 3563 (2015).
- [2] Y. He et al., *Catal. Today* **339**, 48 (2020).
- [3] K. Namba et al., *Proc. Natl. Acad. Sci.* **115**, 7896 (2018).

HALF-METALLIC ELECTRONIC STATES OF BULK-SINGLE CRYSTAL Co_2MnZ ($Z = \text{Ge}$ AND Ga) HEUSLER ALLOYS PROBED BY RESONANT INELASTIC SOFT X-RAY SCATTERING (SX-RIXS) IN A MAGNETIC FIELD

Rie Y. Umetsu¹, Hidenori Fujiwara², Jun Miyawaki³, Rika Kasahara², Takuma Nishioka², Akane Ose², Akira Sekiyama², Yoshihisa Harada^{4,5} and Shigemasa Suga⁶

¹ *Institute for Materials Research (IMR), Tohoku University, Miyagi, Japan*

² *Graduate School of Engineering Science, Osaka University, Osaka, Japan*

³ *National Institutes for Quantum and Radiological Science and Technology (QST), Miyagi, Japan*

⁴ *The Institute for Solid State Physics (ISSP), The University of Tokyo, Tokyo, Japan*

⁵ *Synchrotron Radiation Research Organization, The University of Tokyo, Hyogo, Japan*

⁶ *SANKEN, Osaka University, Osaka, Japan*

Introduction

In our research group, several kinds of Heusler alloys have been investigated by soft x-ray resonant inelastic x-ray scattering (SX-RIXS) measurements in magnetic field to reveal their half-metallic electronic structures [1-3]. The RIXS is a bulk sensitive photon-in and photon-out spectroscopy, and very powerful to investigate such as d - d excitations for open shell $3d$ orbitals and magnetic excitations for spin systems as well as $2p$ - $3d$ transitions in element- and symmetry-specific ways. From comparison between the experimental and theoretical spectra, it was found that the quantitative analyses of the spin-polarized valence band electronic structures related to the half-metallicity would be possible, including such as the Zeeman splitting energy and the spin dependent band gap width across the Fermi level.

RIXS experiments for single crystal of bulk Co_2FeSi Heusler alloy was performed in a previous study. This material has been controversial as a half-metallic ferromagnet, because the given spin polarization is different depending on the theoretical calculation method [4]. The weak structure in the RIXS-MCD spectra between the elastic component and strong fluorescence component suggested the existence of the density of states of Fe- $3d$ orbitals at the Fermi level, suggesting that the obtained results follow the electronic structures given by the generalized gradient approximation (GGA) but not by the local density approximation with considering the electron-electron correlation (LDA+U) [4].

In the present study, we focus on the Co_2MnGa Heusler alloy, which is predicted as one of the Weyl semimetals. It would be very useful to discuss the difference of the electronic structures between such a Weyl semimetal and typical half-metallic materials as Co_2MnSi and Co_2MnGe .

Experiments

a) *Sample preparation*

Single crystals of bulk Co_2MnGe and Co_2MnGa was prepared by Bridgman method after preparing a master alloy by induction furnace melting in Ar gas atmosphere, and annealed at 1273 and 1323 K, respectively. The sample compositions identified by scanning electron microscope-energy dispersive x-ray spectrometry were Co: 49.3, Mn: 24.9, Ge: 25.8 at.%, and Co: 49.4, Mn: 25.2, Ga: 25.4 at.%. Crystal orientations were checked by the Laue method and the specimens were cut in the stripe form with the length of 5 mm along the $\langle 100 \rangle$ with about $1 \times 1 \text{ mm}^2$ cross section. Magnetic properties were investigated with SQUID magnetometer and the magnetic moments converted from the spontaneous magnetizations at 5 K for Co_2MnGe and Co_2MnGa were 4.96 and 4.07 $\mu_B/\text{f.u.}$, respectively, and the Curie temperatures measured by differential scanning calorimetry were 913 and 697 K, respectively.

b) *RIXS experiment*

RIXS experiments were performed using a high-resolution soft x-ray emission

spectrometer installed at the end of the BL07LSU of SPring-8. The specimens were fractured in a VUV chamber. The RIXS spectra for Mn $2p$ core excitation were measured with use of the right and left helicity circularly polarized light at room temperature. A permanent magnet with the field of 0.25 T was installed in the chamber and arranged as the x-ray incidence direction and the magnetic field direction become parallel.

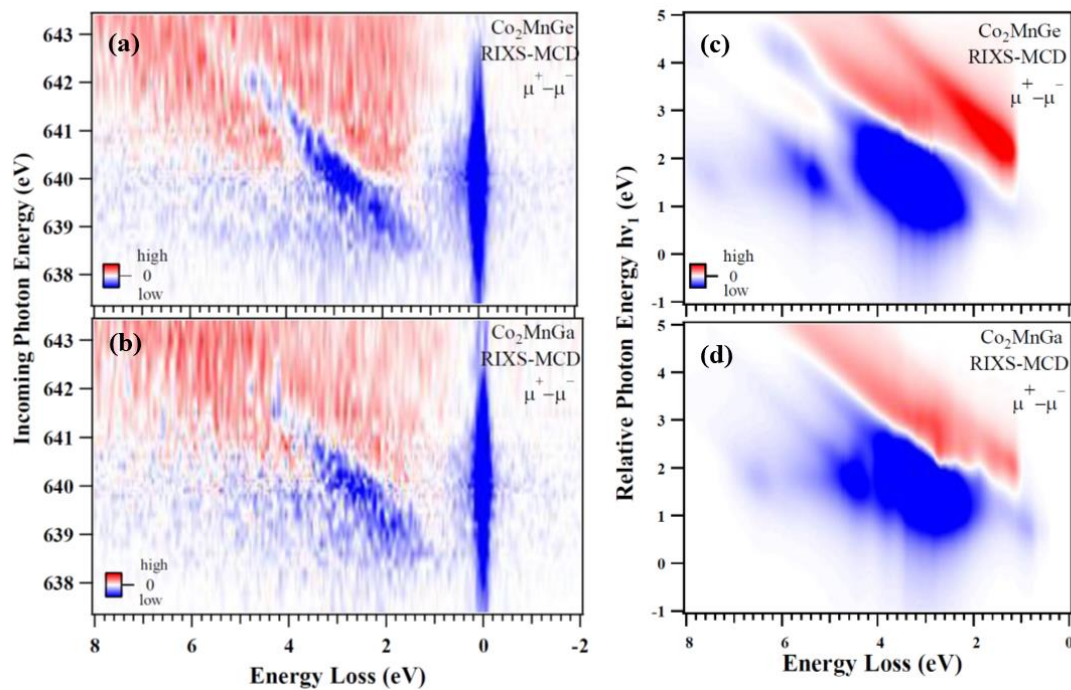
Results

Figures (a) and (b) show the intensity maps of RIXS-MCD spectra obtained by parallel (μ^+) and antiparallel (μ^-) configurations between the photon helicity and the magnetic field at incoming photon energy, for Mn L_3 edge in Co_2MnGe and Co_2MnGa , respectively. Strong RIXS-MCD signals are recognized in both the elastic and fluorescence components. The former is observed at the zero-energy loss and the latter shifts linearly with the excitation photon energy. The fluorescence MCD signals contain both negative (blue) and positive (red) signs. The blue area is dominant in lower incoming photon energy regions, and the red area dominates in higher energy regions.

Figures (c) and (d) are intensity maps obtained by calculated spectra of RIXS-MCD for Mn L_3 edge in Co_2MnGe and Co_2MnGa , respectively. The features pointed out above are qualitatively reproduced. In details, the distributions of the RIXS-MCD of the fluorescence components for Co_2MnGa are slightly shifted to lower energy loss regions, reflecting the different number of the electrons in the valence band between Co_2MnGa and Co_2MnGe .

REFERENCES

- [1] K. Nagai, H. Fujiwara *et al.*, Phys. Rev. B 97 (2018) 035143.
- [2] R.Y. Umetsu *et al.*, Phys. Rev. B 99 (2019) 134414.
- [3] H. Fujiwara *et al.*, Sci. Rep., 11 (2021) 18654.
- [4] K. Nishimoto, H. Fujiwara, R.Y. Umetsu *et al.*, in preparation.



Figs. Intensity maps of RIXS-MCD spectra for L_3 edge in Co_2MnGe (a) and Co_2MnGa (b). The RIXS spectra recorded for parallel (μ^+) and antiparallel (μ^-) configurations of the photon helicity. Calculated spectra by Kramers-Heisenberg formula based on the GGA for Co_2MnGe (c) and Co_2MnGa (d).

KINETIC SQUARE SCHEME IN OXYGEN-REDOX BATTERY ELECTRODES

Masashi OKUBO

Department of Electrical Engineering and Bioscience, School of Advanced Science and Engineering, Waseda University

The rapid market growth of electric vehicles (EVs) has significantly increased the industrial demands for their improved performance, such as longer driving distance, longer calendar life, and lower cost. For example, the driving distance of an EV is determined by the energy density of in-vehicle lithium-ion batteries (LIBs). However, current LIBs possess an unsatisfactory gravimetric energy density of 200–250 Wh/kg, powering typical EVs for 300–400 km per charge, which is below most consumers' requirements. Thus, increasing the energy density of LIBs is crucial for the widespread use of EVs. The energy density of LIBs is limited in part by the specific capacity of the positive electrode (cathode) material. Conventional cathode materials, i.e., layered transition-metal oxides LiMO_2 (M = transition metal), deliver a modest capacity of approximately 160 mAh/g, where the dominant mechanism of charge compensation for lithium-ion (de)intercalation is the valence change of the transition metal. Further increase in the cathode capacity requires an additional redox center. To activate redox reactions of oxide ions (oxygen redox), lithium-rich transition-metal oxides have been extensively studied for over a decade as they deliver much larger reversible capacities (> 200 mAh/g).

This work focuses on O2-type lithium-rich layered transition-metal oxides as cathode materials with structural integrity (O2: lithium ions occupy octahedral sites between the MO_2 layers and the packing arrangement of the oxide ions is ABCBA), which is an emerging class of oxygen-redox electrode materials. In the O2-type oxides, the structural degradation upon cycling is suppressed because migration of M to the Li^+ layer is unfavorable: M in a Li^+ layer

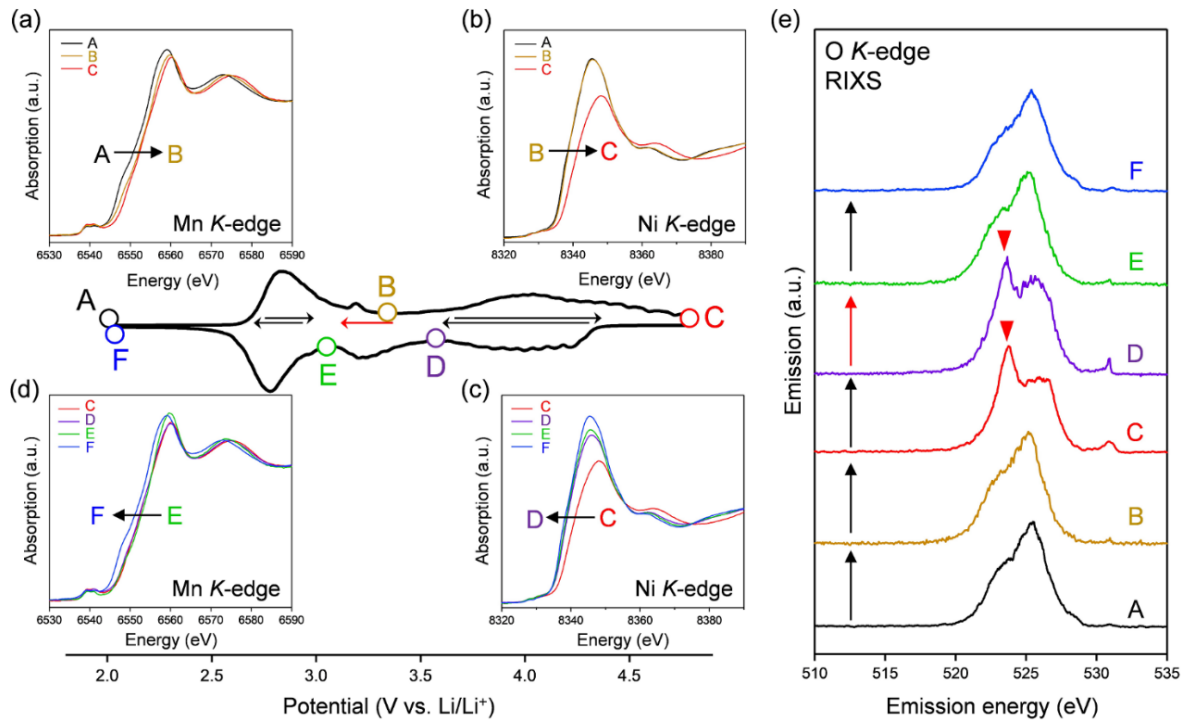


Figure 1. Redox couples in O2-Li_{1.12-y}Ni_{0.17}Mn_{0.71}O₂. dQ/dV plot during the second cycle at a charge/discharge rate of C/20. (a–d) Ex situ Mn and Ni K-edge X-ray absorption spectra upon charge and discharge. (e) Ex situ O K-edge resonant inelastic X-ray scattering (RIXS) spectra excited by an incident photon energy of 531 eV.

suffers from strong Coulombic repulsion from face-sharing M^{n+} in an adjacent MO_2 layer. Moreover, O2-type Li-rich layered oxides exhibit negligible O2 gas release. As a consequence, O2-Li_{1.12-y}Ni_{0.17}Mn_{0.71}O₂ provides a large reversible capacity greater than 200 mAh/g with minimal voltage decay and capacity fading upon cycling.

O2-Li_{1.12-y}Ni_{0.17}Mn_{0.71}O₂ was synthesized by the Na⁺/Li⁺ ion-exchange method using P2-Na_{0.71}[Li_{0.12}Ni_{0.17}Mn_{0.71}]O₂ as a precursor. The powder X-ray diffraction pattern of O2-Li_{1.12-y}Ni_{0.17}Mn_{0.71}O₂ shows Bragg peaks indexed to a hexagonal system (space group: *P6₂mc*, typical of the O2 phase), indicating the successful transformation of the P2-type sodium layered oxide to the O2-type lithium layered oxide. Indeed, a high-angle annular dark-field scanning transmission electron microscopy image confirms the O2-type stacking of the transition-metal layers. Galvanostatic charge/discharge measurements show that O2-Li_{1.12-y}Ni_{0.17}Mn_{0.71}O₂ delivers a large discharge capacity of approximately 210 mAh/g, exceeding the M-redox capacity (193 mAh/g). After 80 cycles, 98% of the discharge capacity in the second cycle is retained, while the decay of the average discharge voltage is negligibly small (< 5 mV). Typically, conventional O3-type oxygen-redox layered oxides exhibit structural degradation initiated by the migration of M to Li⁺ layers. In contrast, in O2-type layered oxides, M^{n+} ions migrated to Li⁺ layers would be subjected to strong Coulombic repulsion from face-sharing M^{n+} ions in the adjacent MO_2 layers, such that the migration of M would be energetically unfavorable to mitigate both capacity fading and voltage decay during the charge/discharge cycles.

To identify the redox center, ex situ X-ray absorption/emission spectroscopy measurements were conducted. Mn and Ni K-edge X-ray absorption near-edge structure (XANES) spectra during the second cycle show that the redox reaction at 2.8 V vs. Li/Li⁺ corresponds to the oxidation and reduction of Mn while that at 3.9 V vs. Li/Li⁺ can be attributed to the oxidation and reduction of Ni (Figure 1a-d). These attributions (Mn and Ni redox reactions at 2.8 and 3.9 V vs. Li/Li⁺, respectively) are double-confirmed by Mn and Ni L-edge absorption spectra. After charging to 4.8 V vs. Li/Li⁺, O K-edge X-ray absorption spectroscopy shows the emergence of new absorption at approximately 531 eV, while resonant inelastic X-ray scattering (RIXS) spectra with the incident photon energy of 531 eV show intense emission at 524 eV (Figure 1e), both of which are characteristic features of charged oxygen-redox electrode materials. Thus, the anodic dQ/dV peak at 4.5 V vs. Li/Li⁺ corresponds to the oxidation of oxide ions. These signals for oxidized oxygen do not completely disappear even after discharging to 3.6 V vs. Li/Li⁺. Instead, the disappearance is confirmed after discharging to 3.1 V vs. Li/Li⁺. Considering the similar emission peaks observed for Li₂O₂, CaO₂, and O₂ molecule, dimerized oxygen species O₂ⁿ⁻ (n = 0 or 2) exists in charged O2-Li_{1.12-y}Ni_{0.17}Mn_{0.71}O₂ at 4.5 V. It is noteworthy that an enhancement in the elastic peak region was observed after charge (spectrum C and D in Figure 1e). A possible explanation is the Raman scattering arising from the vibrational transition of O–O bond although its origin is still under debates.

Overall, the O–O dimerization in O2-Li_{1.12-y}Ni_{0.17}Mn_{0.71}O₂ can be summarized by the square scheme. Upon charge, O²⁻ with non-bonding 2p states is oxidized to O⁻ above 4.2 V vs. Li/Li⁺. At the early stage of oxygen oxidation, O⁻ is thermodynamically more favorable than O₂²⁻. However, with further oxygen oxidation, the over-oxidized oxide ions dimerize to form O₂²⁻.

REFERENCES

- [1] K. Kawai, X. M. Shi, N. Takenaka, J. Jang, B. Mortemard de Boisse, A. Tsuchimoto, D. Asakura, J. Kikkawa, M. Nakayama, M. Okubo, A. Yamada, *Energy Environ. Sci.* **2022**, *15*, 2591-2600

ORBITAL TORQUE IN CoFe/Cu/Al₂O₃: INVESTIGATION ON THE LARGE TORQUE WITHOUT HEAVY ELEMENT

Junyeon KIM

Center for Emergent Matter Science, RIKEN

Introduction

Recently, sizeable orbital torque is experimentally observed in CoFe/Cu/Al₂O₃ stacks [1]. This orbital torque is indeed caused by the generation of nonzero orbital angular momentum (OAM) at the Cu/Al₂O₃ interface (Fig. 1). Nowadays, the orbital torque greatly draws interest for the spin accumulation since there is no clear restrictions on materials for the nonzero OAM generation. It is apparently contrast to the spin angular momentum generation which is mainly shown in material systems consisted of heavy elements.

A recent theoretical study reports that the orbital hybridization between the *p*-orbital of oxygen atom and the *d*-orbital atom serves the formation of a chiral orbital texture by orbital Rashba effect (Fig. 1(a)) [2]. For further understand on the nonzero OAM generation at the Cu/Al₂O₃ interface, we require detailed material characterization. Also observation of a modulation of the energy spectrum by a generation of nonzero OAM is also desired.

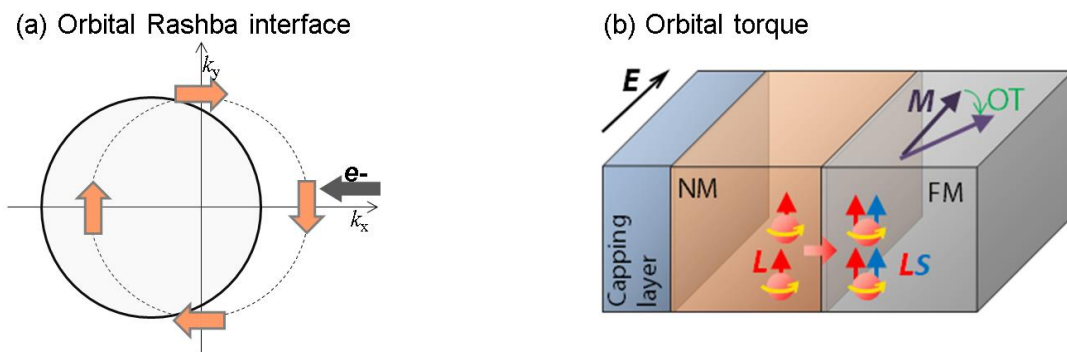


Fig. 1(a) Excess OAM generation at a chiral orbital texture. Here the chiral orbital texture is formed by orbital Rashba effect. (b) Orbital torque in FM/Cu/Oxide system.

Experimental method

For the observation of the Cu/Al₂O₃ interface, L-edge X-ray magnetic circular dichroism (XMCD) was utilized. Nominally, the 3*d* orbital state of Cu is known to be fully occupied. However Grioni et al. claimed that there is still unoccupied 3*d* orbital state for Cu due to a hybridization between *s* state and *d* states [3]. And the number of unoccupied 3*d* orbital state can be promoted by formations of compounds such as CuOx. Thus we could expect the L2, 3 edge X-ray absorption.

As a first, we attempt to obtain the energy spectrum nearby the Cu/Al₂O₃ interface. Next, we also attempt to obtain a clue of the nonzero OAM generation by turning on/off the charge current.

The observation was performed in superconducting magnet magneto-optical observation system in the free board. The CoFe/Cu/Al₂O₃ and the Cu/Al₂O₃ stacks are electronically connected by the silver paste. And the observation was carried out by high speed switching of the circularly polarized light and total electron yield (TEY) technique. To optimize the sample condition, 2, 5, 7, 10 nm of Al₂O₃ was tested considering with the detection length of the TEY technique (~10 nm).

Experimental results and discussion

As shown in Fig. 2, the energy spectrum is successfully obtained by the TEY technique for the CoFe/Cu/Al₂O₃ and the Cu/Al₂O₃ stacks. Here the Cu peak is clearly found for all the stacks, but the CuO or Cu₂O peak is not shown. It asserts that formation of Cu oxide mostly does not occur, although temperature would drastically increase during the Al₂O₃ layer deposition. We think the Al₂O₃ is extremely stable as showing large Gibbs free energy, thus it is not easily decomposed even in extreme conditions. We think this result is quite helpful for further analysis of the interfacial condition. We also attempt to observe the nonzero OAM generation by the XMCD, but it is not successful due to a drastic Joule heating during the observation..

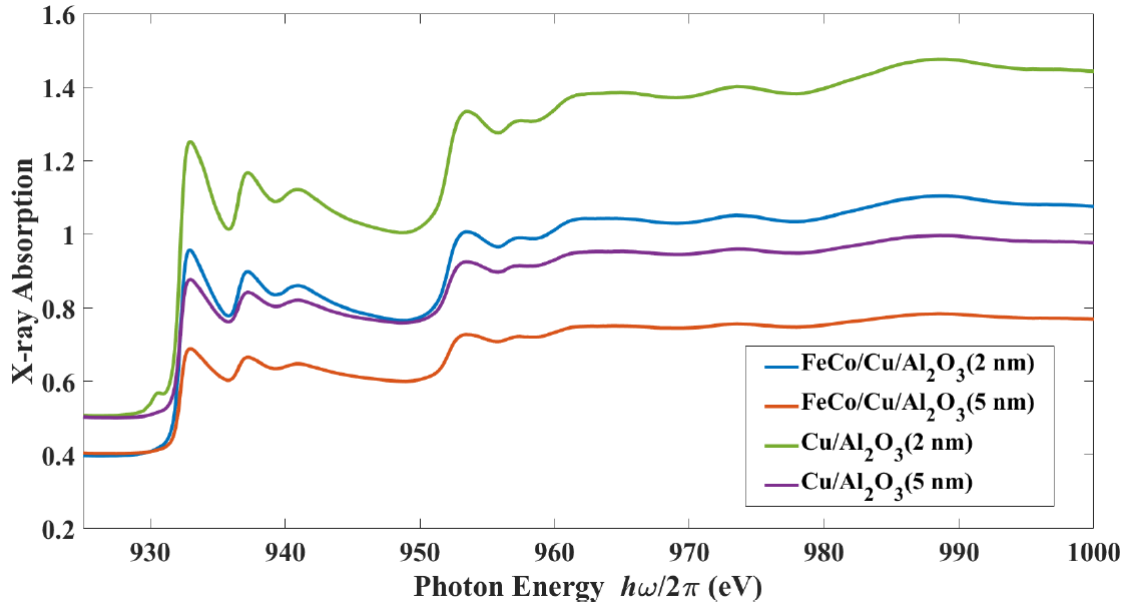


Fig. 2 Energy spectrum for the several CoFe/Cu/Al₂O₃ and the Cu/Al₂O₃ stacks observed by the TEY technique.

REFERENCES

- [1] J. Kim *et al.* Phys. Rev. B **103**, L020407 (2021).
- [2] D. Go *et al.*, Phys. Rev. B **103**, L121113 (2021).
- [3] M. Grioni *et al.*, Phys. Rev. B **39**, 1541 (1989).

MAGNETIC STATE OF VNB₃S₆ DETERMINED BY X-RAY MAGNETIC CIRCULAR DICHROISM

Masafumi HORIO¹, Tomoaki SENOO¹, Tetsuya WADA¹, Yasuyuki HIRATA²,
Shota OKAZAKI³, Takao SASAGAWA³, Iwao MATSUDA¹

¹*The Institute for Solid State Physics, The University of Tokyo*

²*Department of Applied Physics, National Defence Academy*

³*Materials and Structures Laboratory, Tokyo Institute of Technology*

Transition metal dichalcogenides TX₂ (T = Mo, Nb, W, X = S, Se, Te) are model semiconductors with various intriguing aspects such as charge ordering, Weyl semimetallicity, valleytronics, Mottness, and superconductivity, and have established themselves as a major research field in condensed matter physics. In the 1970s and 1980s, there has been a trend to extend the physical properties of TX₂ by intercalating 3d metal M into TX₂. It was demonstrated that magnetic ordering appears with a strong dependence on the inserted 3d transition metal [1]. One of the reasons why the MT₃X₆ system attracted much attention is that the intercalation of Cr into NbS₂ results in a helical magnetic structure called chiral soliton lattice. Recently, due to the coexistence of the space-inversion and time-reversal symmetry breaking, the MT₃X₆ system has attracted a renewed attention from a topological point of view. In particular, VNb₃S₆, which is known to be ferromagnetic below T_c~50 K, has been predicted by first-principles calculations to host a Weyl point in the ferromagnetic phase and exhibit an anomalous Hall effect [2]. The prediction has triggered intense efforts to synthesize high-quality MT₃X₆ single-crystal samples and to evaluate their physical properties. Surprisingly, a recent neutron scattering study [3] reported that VNb₃S₆ is not ferromagnetic but in a canted antiferromagnetic state, contrary to the understanding accepted for 40 years [1]. Under these circumstances, it is required to precisely determine the intrinsic magnetic state of VNb₃S₆, excluding the possibility of impurities, in order to elucidate the origin of the anomalous Hall conductivity of VNb₃S₆.

We have therefore performed x-ray absorption spectroscopy (XAS) and x-ray magnetic circular dichroism (XMCD) measurements of VNb₃S₆ single crystals. The samples were cleaved in air and immediately introduced into an ultra-high vacuum chamber equipped with a superconducting magnet at SPring-8 BL07LSU. The measurements were conducted in the total electron yield mode at T = 30 K, below the magnetic transition temperature, under a magnetic field of 3 T. Both normal and grazing (20 degree) incidence conditions were employed.

Figure 1 shows the XAS and XMCD spectra of VNb₃S₆ measured with the grazing incidence condition. Whereas transition-metal ions intercalated into NbS₂ have been usually assumed to be trivalent, the broad absorption spectrum without well-defined pre-edge does not seem compatible with V³⁺ [4-6]. Instead, it is more consistent with intermediate valence state lower than 3+, as seen in systems like V_{0.1}(Bi_{0.32}Sb_{0.68})_{1.9}Te₃ [7]. This deviation suggests strong hybridization of V orbitals with surrounding NbS₆ layers. The spectral shape of obtained XMCD spectrum is also close to that of V_{0.1}(Bi_{0.32}Sb_{0.68})_{1.9}Te₃ [7] rather than those of the V³⁺ compounds [4-6], further supporting this conclusion. Due to the overlap of L₂ and L₃ absorption edges, the sum rule cannot be applied for V L-edge XMCD and hence it is not straightforward to quantitatively evaluate the magnetic moment. Nevertheless, a naive comparison with a cluster calculation [6] yields an approximate value of ~0.4 μ_B which is one order of magnitude smaller than the values from previous magnetization measurements which reported ferromagnetism [1]. The magnitude of the XMCD signal did not substantially change under the normal incidence setup (not shown). The obtained results are therefore in favor of

canted antiferromagnetism rather than the ferromagnetism. Combined with our ongoing photoemission measurements, the present work will establish the electronic structure of VNb_3S_6 and set a starting point to discuss the origin of anomalous Hall conductivity.

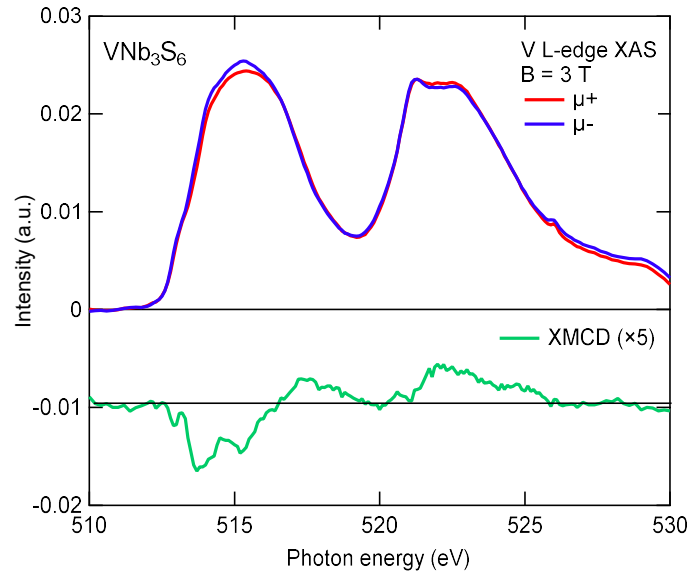


Fig. 1: XAS and XMCD spectra of VNb_3S_6 measured at the incidence angle of 20 degree and at $T = 30$ K under the magnetic field of 3 T.

REFERENCES

- [1] S.S.P. Parkin *et al.*, *Philos. Mag. B* **41**, 65 (1980).
- [2] T. Inoshita *et al.*, *Phys. Rev. B* **100**, 121112(R) (2019).
- [3] K. Lu *et al.*, *Phys. Rev. Mater.* **4**, 054416 (2020).
- [4] M. Abbate *et al.*, *J. Electron Spectrosc. Relat. Phenom.* **62**, 185 (1993).
- [5] M. Horio *et al.*, *J. Phys. Spc. Jpn.* **87**, 105001 (2018).
- [6] Y. Nonaka *et al.*, *Phys. Rev. B* **97**, 205126 (2018).
- [7] T. R. F. Peixoto *et al.*, *npj Quantum Materials* **5**, 87 (2020).

MEASUREMENT OF X-RAY MAGNETIC LINEAR DICHROISM BY ROTATING POLARIZATION ANGLE OF SOFT X-RAY GENERATED BY A SEGMENTED CROSS UNDULATOR

Masafumi HORIO¹, Yoshiki KUDO¹, Toshihide SUMI¹, Tetsuya WADA¹,
Yasuyuki HIRATA², Kohei YAMAMOTO³, Takuo OHKOCHI^{4,5}, Toyohiko KINOSHITA⁴,
Iwao MATSUDA¹

¹*The Institute for Solid State Physics, The University of Tokyo*

²*Department of Applied Physics, National Defence Academy*

³*Department of Materials Molecular Science, Institute for Molecular Science*

⁴*Japan Synchrotron Radiation Research Institute (JASRI)*

⁵*RIKEN SPring-8 Center*

X-ray magnetic linear dichroism (XMLD) is a widely used technique for studying magnetic anisotropy. By measuring the absorption of soft X-rays while changing the relative angle between the linear polarization of the soft X-rays and the crystal axis, information about the orientation of the spin of the magnet can be obtained. Because of the limitation in controlling the polarization of soft X-rays, the sample is conventionally rotated around a certain axis to perform XMLD measurements. Therefore, the measurement conditions were limited, especially when measuring non-uniform samples under *operando* conditions. In the present study, we report a novel method for XMLD measurements operated by continuously rotating the linear polarization angles while samples are fixed.

At BL07LSU at SPring-8, continuous polarization modulation of a soft X-ray beam was achieved using a segmented cross undulator [1]. The source consists of eight insertion devices (IDs) and seven phase shifters; the ID segments are a horizontal figure-8 undulator and a vertical figure-8 undulator, which generate horizontal and vertical linear polarization, respectively. To generate linear polarization at arbitrary angles, we first prepared two sets, set A and set B, consisting of two sets of horizontal and vertical figure-8 undulators, as shown in Fig. 1. By adjusting phase shifters #1-3 and #5-7, each set can generate right or left circular polarization. For example, the four undulators in the front (set A) generate right circular polarization, while the four undulators in the rear (set B) generate left circular polarization. The roles of Set A and Set B can be interchanged. The two waves of right and left circular polarization are then combined to produce linear polarization. There, the rotation angle of the linearly polarized light was controlled by changing the phase between Set A and Set B using a phase shifter (PS#4 in Fig. 1). As a sample, we prepared a single crystal of NiO (Néel temperature $T_N = 523$ K). The crystal was cleaved with a knife to expose the (001) plane and fixed on a copper plate with carbon tape. The sample was then introduced into an ultra-high vacuum chamber. Here, in addition to the conventional XAS/XMLD measurements, a novel "rotational" XMLD measurement was performed. All spectra were recorded at room temperature in the total electron yield mode.

Figure 2(a) shows the Ni L absorption edge XAS spectrum of a NiO crystal, measured with horizontal and vertical polarization with an incident angle of 80° from the (001) surface [see Fig. 1]. The XAS spectrum was normalized by the integrated intensity in the range 878-881 eV. The XMLD spectrum of the NiO crystal was obtained by taking the difference between the XAS spectra recorded with horizontal and vertical linear polarization [Fig. 2(b)]. Linear dichroism is clearly found. Focusing on the L2a and L2b peaks in the figure, we see that the L2a peak is enhanced by horizontal polarization and the L2b peak by vertical polarization. This contrasting response to light polarization gives rise to the XMLD signal plotted in Fig.

2(b). These results are consistent with previous L-absorption edge XMLD experiments on NiO [2] and suggest that the in-plane spin component is dominant on the cleaved NiO (001) surface.

After confirming the performance of the conventional method, we present the results of XMLD measurements while rotating the linear polarization angle. Here, we focus on the Ni L2 absorption edge peaks, L2a and L2b. The photon energy incident on these peaks was fixed, and the XAS intensity was detected while continuously changing the angle of linear polarization during the measurement. Figures 2(c) and (d) show the results. The intensity varies with a period of π , indicating a clear contrast in XMLD. The inversion of the order of the ID section (red and blue curves in the figure) also confirms that the signal is dichroic. Figures 2(c) and (d) also show that the dependence is opposite between L2a and L2b, as expected for the XMLD signal displayed in Fig. 2(b).

The advantage of this rotation method is that the linear dichroism signal is more reliable because the linear polarization angle dependence is tracked while the sample position is fixed. This method is useful for detecting the small electronic and magnetic anisotropies often found in quantum materials. Fixing the sample position also allows operando XMLD experiments, where sample size and rotational motion are severely restricted.

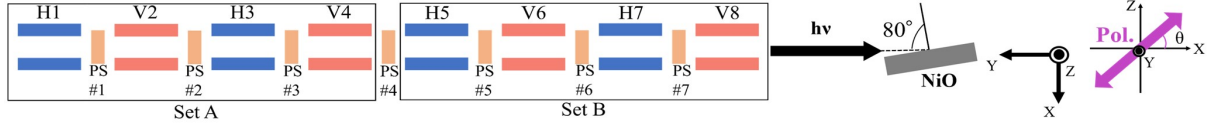


Fig. 1: A schematic of the segmented cross undulator and the measurement configuration. H and V denote IDs for horizontal and vertical polarization, respectively. Linearly polarized soft X rays travel along the Y axis and the polarization angle θ is varied within the X-Z plane.

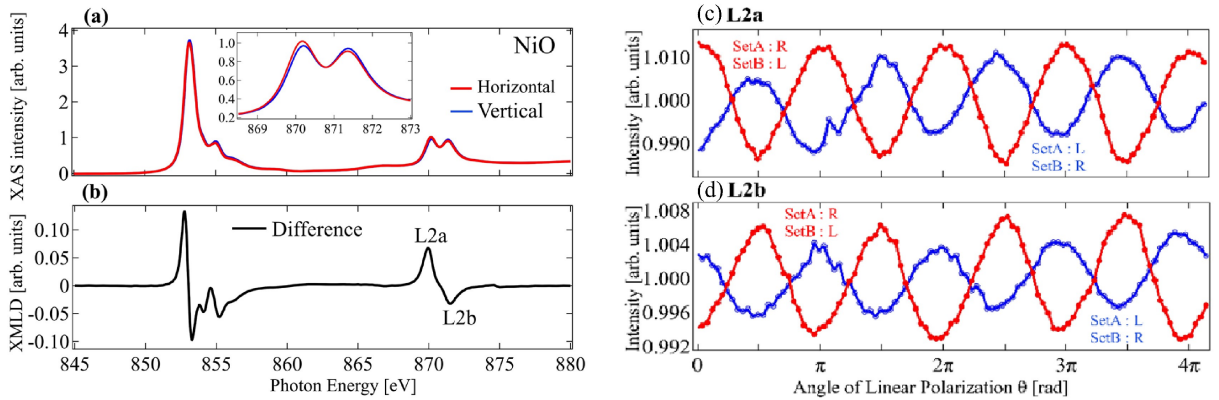


Fig. 2: Ni L-edge XMLD of NiO taken at an incident angle of 80 degree. (a) XAS measured with horizontal and vertical polarization. (b) XMLD obtained by taking the difference of two curves in (a). (c), (d) Rotational XMLD measured at L2a and L2b peaks [see (b)], respectively, plotted against linear polarization angle θ . For the red (blue) curve, undulator set A produces right (left) polarization while set B produces left (right) polarization.

REFERENCES

- [1] S. Yamamoto et al., J. Synchrotron Rad. **21**, 352 (2014).
- [2] G. van der Laan *et al.*, Phys. Rev. B **83**, 064409 (2011).
- [3] H. Ohldag *et al.*, Phys. Rev. Lett. **86**, 2878 (2001).

DEVELOPMENT OF ANGLE-RESOLVED SOFT X-RAY EMISSION SPECTROSCOPY

Naoya Kurahashi¹, Jun Miyawaki¹, Kosuke Yamazoe² and Yoshihisa Harada¹

¹*Synchrotron Radiation Laboratory, The Institute for Solid State Physics, The University of Tokyo*

²*Japan Synchrotron Radiation Research Institute*

Soft X-ray emission spectroscopy is a powerful technique to observe the valence electronic state of occupied orbitals, as it involves emission of excess energy as light when a valence electron relaxes into a core hole generated by the soft X-ray excitation. The measurement under ambient pressure including wet condition is realized by using X-ray transmission windows such as silicon nitride. Photoelectron spectroscopy is another method for directly observing occupied electronic states, and it is possible that photoelectron spectroscopy and emission spectroscopy provide complementary information, as exemplified by the results of bulk water measurements [1]. While soft X-ray emission spectroscopy can approach samples in a variety of environments, it tends to have a broad natural width of the spectrum, due to the short lifetime of the core hole. Because of this, it may not be possible to completely separate the electronic states only by the emission energy but a method utilizing other physical parameters for assigning electronic states is required.

Since photoelectron spectroscopy for atoms and molecules has long been used to study photo-excitation dynamics, there has been a need for a method to understand the electronic excitation states. To solve this problem, a photoelectron velocity mapping method[2] has been developed that enables simultaneous observation of the kinetic energy and emission angle of photoelectrons. In the process of photoelectron emission, the orbital angular momentum of electrons changes by ± 1 according to the law of conservation of angular momentum ($\Delta l = \pm 1$). For example, electrons from the s -orbital are emitted in the form of p -orbitals, while those in the p -orbital are emitted as a superposition of s - and d -orbitals. As a result, by measuring the kinetic energy and emission angle distributions of photoelectrons, information on the energy levels and angular momenta of the original orbitals can be obtained, which enables precise assignment of electron orbitals.

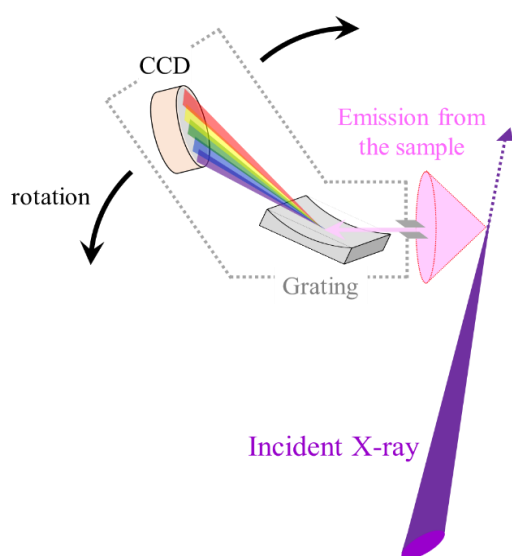


Fig. 1 Schematic of soft X-ray emission angular anisotropy measurement. The incident light and emission points were fixed and the spectrometer was rotated in the horizontal plane.

As in X-ray emission spectroscopy, $\Delta l = \pm 1$ should hold and the angular momentum change of the electron orbitals is expected to be emitted in the form of light. Therefore, the soft X-ray emission is expected to be anisotropic, reflecting the symmetry of the electron orbitals. Therefore, we planned to observe the angular anisotropy of soft X-ray emission from a gaseous sample.

In emission spectroscopy, a portion of the light emitted from a sample is cut off and dispersed by a spectrometer. In a soft X-ray emission angular anisotropy experiment, the angular anisotropy of soft X-ray emission from a sample can be observed by performing emission spectroscopy measurements with linearly polarized light incident on the sample and the entire grating and detector rotated around the sample (Fig. 1). By using a gas-phase sample, the angular emission anisotropy is considered to depend only on the angle between the

molecular axis and the electric field plane of light and the symmetry between the core-excited intermediate and final states of the molecule, making it easy to compare with theoretical calculations. Due to the trade-off between energy resolution and detection efficiency in emission spectroscopy, and the low efficiency of X-ray fluorescence for light elements, soft X-ray emission spectroscopy for gaseous samples has been considered difficult. To solve this problem, we have developed a method to increase the density of a target gaseous element at the sample position. In this method, X-ray is introduced very close to the sample introduction nozzle (within a few- μm) by devising the shape of the sample introduction nozzle, allowing emission measurement in a high-density region before the sample diffuses. This method achieves a signal intensity 100 times higher than that of conventional gas nozzles, while maintaining a high vacuum in the chamber by reducing the absolute amount of sample. We performed soft X-ray emission observation of oxygen gas and succeeded in the first soft X-ray emission angle anisotropy measurement of gaseous molecules (Fig. 2). The pressure in the vacuum chamber remained at around 10^{-4} Pa even though 100 kPa pure-oxygen gas was introduced, and no influence on the light source or other devices was observed.

When the excitation energy was 530.8 eV, which is the $1s\text{-}\sigma_u$ to $2p\text{-}1\pi_g^*$ excitation (${}^3\Sigma_g^- \rightarrow {}^3\Pi_u$), and the polarization was horizontal, the ${}^3\Sigma_g^-$ signal intensity was dependent on the angle of the spectrometer. The ${}^3\Sigma_g^-$ emission from ${}^3\Pi_u$ is stronger in the direction perpendicular to the polarization direction of the incident light. On the other hand, no clear angular anisotropy was observed for ${}^3\Pi_g$ emission; both ${}^3\Sigma_g^-$ and ${}^3\Pi_g$ emission angular anisotropies differed from theoretical predictions and from the results of photoelectron angular anisotropy. The presence

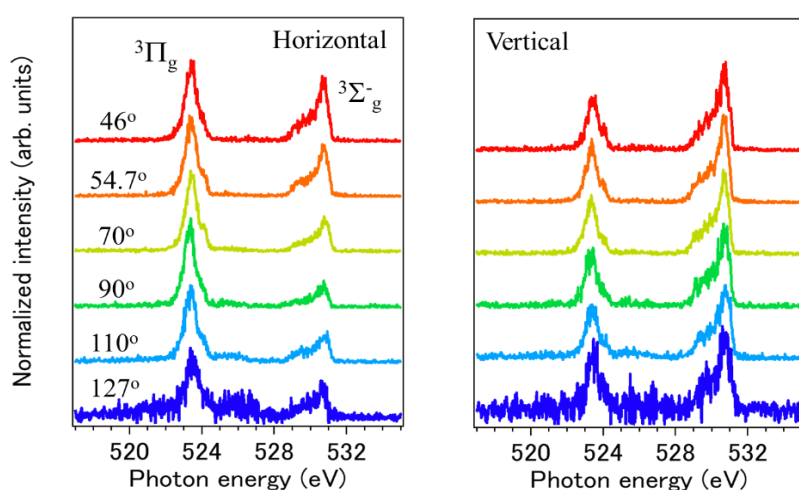


Fig. 2 Soft X-ray emission angle anisotropy measurements of oxygen excited at 530.8 eV. The angle in the figure indicates the angle between the optical axis of the incident light and the monochromator.

of a relatively long-lived component in ${}^3\Sigma_g^-$ may have weakened the information on angular anisotropy due to molecular rotation[3]. The results of the present study were compared with the theoretical calculations.

No angular anisotropy was observed in any of the peaks when the polarization was set to vertical. This indicates that the measurement system maintains cylindrical symmetry in vertical polarization. This means that the sample emission

occurred at the center of rotation of the spectrometer.

With this research, we succeeded in a windowless experiment of soft X-ray emission spectroscopy, and also succeeded in measuring the soft X-ray emission angular anisotropy. We would like to compare our understanding of the measurement results with theoretical calculations.

REFERENCES

- [1] T. Fransson *et al.*, *Chem. Rev.*, 116, 7551 (2016).
- [2] T. Suzuki, *Annu. Rev. Phys. Chem.*, 57, 555 (2006).
- [3] J.-E. Rubensson *et al.*, *J. Electron Spectros. Relat. Phenomena*, 185, 294 (2012).

CHARGE EXCITATION RESEARCH ON THE T* PHASE HOLE-DOPED CUPRATES BY RESONANT SOFT X-RAY SCATTERING

Xie PEIAO¹, Shinnosuke KITAYAMA¹, Takanori TANIGUCHI¹, Hisao KIUCHI², Kenji ISHII³, and Masaki FUJITA¹

¹ Institute for Materials Research, Tohoku University, Sendai 980-8577, Japan

² Institute for Solid State Physics, University of Tokyo, Kashiwa 277-8581, Japan

³ Synchrotron Radiation Research Center, National Institutes for Quantum and Radiological Science and Technology, Hyogo 679-5148, Japan

Recently, the momentum-dependent charge excitations have been found to exist on the hole-doping $\text{La}_{2-x}(\text{Br}, \text{Sr})_x\text{CuO}_4$ from the O K -edge resonant inelastic x-ray scattering (RIXS) experiment [1]. The results showed the outwardly dispersive mode which contains the same behaviors as the NCCO L_3 -edge RIXS spectrum [2,3]. The authors ascribed it's come from the charge excitations. However, the existence of the dispersive mode originating from charge excitations in all cuprate families is still under debate [4,5]. In this experiment, we first performed the charge excitations study for another 214-type cuprate — the T* phase family, which contained CuO_5 pyramid coordination formed by alternate stacks of rock-salt layers (T phase) and fluorite layers (T' phase). The SC state of T* phase cuprates emerged after oxidation annealing (O-AN) under high pressure to repair the oxygen deficiency around the apical site. Due to such a unique crystal structure, this research may inspire us further understand the physical nature of charge excitations.

The measurement was performed on the beamline BL07LSU at SPring-8. The $\text{SmLa}_{0.75}\text{Sr}_{0.25}\text{CuO}_4$ (SLSCO) of the as-sintered (AS) samples were grown by the traveling solvent floating zone (TSFZ) method with 2.5 atoms of oxygen. The quality of the crystal was checked by the x-ray back-scattering Laue method. The representative Laue pattern taken with the x-ray beam parallel to $[0, 0, 1]$ crystalline axis is shown in Fig. 1 (a). The oxygenized (O-AN) samples were prepared by annealing the AS samples in oxygen gas under $\sim 46\text{MPa}$ at 500°C for 80 h. Fig. 1 (b) shows the magnetic susceptibility of the O-AN sample. We tuned the incident photon energy for the RIXS measurements to the hole peak value at $\sim 528.3\text{eV}$ by scanning the total fluorescence yield. In this measurement, we set the c axis of AS and O-AN samples kept parallel to the horizontal scattering plane. The samples were cleaved in the air just before the measurements.

Figures 2 (a) – (d) show the O K -edge RIXS spectra and image plot for both AS and O-AN samples with the whole \mathbf{q} range in our measurement. We observed the RIXS signal (grey line) of T*-type cuprates and the oxidation annealing effect on the charge excitations for the first time. The signal was obtained by subtracting the elastic and fluorescence peak, and all the data were normalized by the integrated intensity of fluorescence at $\mathbf{q} = (0.1, 0)$ of the O-AN sample. Because it was difficult to fit the RIXS signal systematically, the spectral intensity over 90% of the maximum has been chosen as the peak's region. Notably, the elastic peak of O-AN samples contained an obvious additional peak at around 0.2 - 0.3 eV. We fitted only elastic peak by Gaussian function to extract such a peak. For

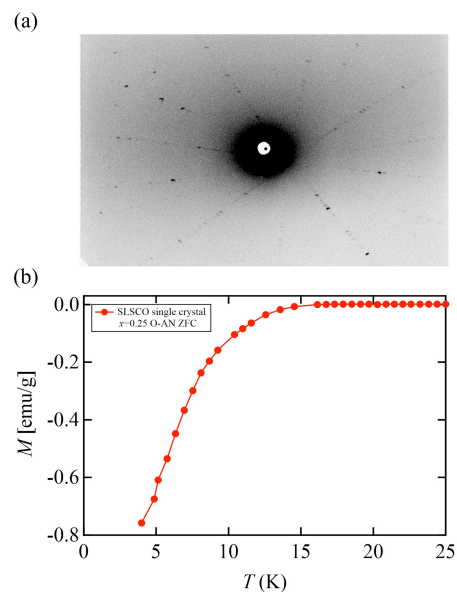


Fig. 1 (a) Laue pattern and (b) magnetic susceptibility of O-AN $\text{SmLa}_{0.75}\text{Sr}_{0.25}\text{CuO}_4$.

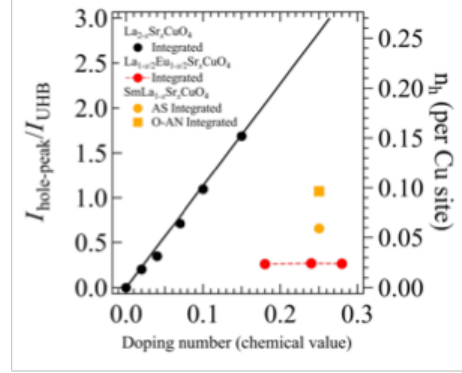
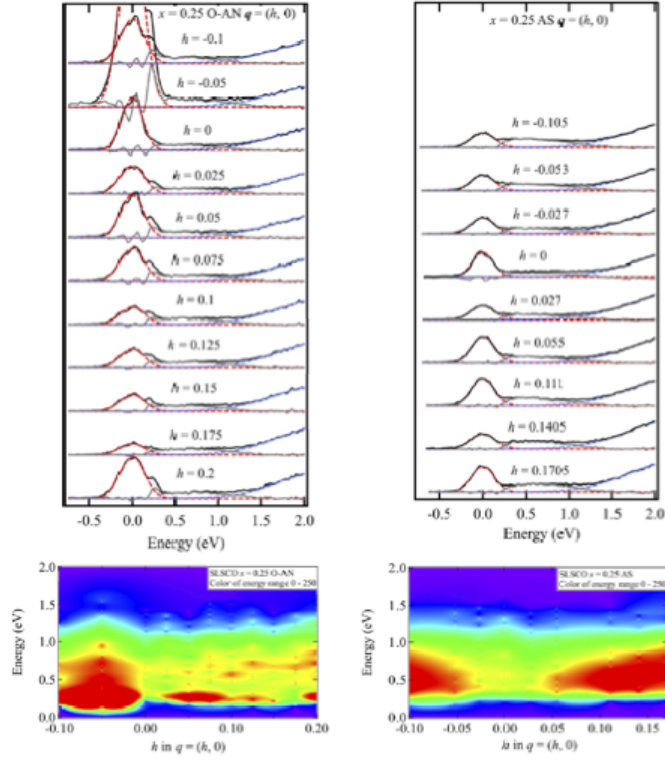


Fig 2. RIXS spectra and image plots of (a), (c) AS and (b), (d) O-AN $\text{SmLa}_{0.75}\text{Sr}_{0.25}\text{CuO}_4$. (e) Doping dependence of the ratio value from the integral intensity of hole and upper Hubbard band peaks, the LSCO results plotted in the black line as a reference.

both O-AN and AS samples, the RIXS signal was much weaker than the LSCO in the previous report with faintly momentum-dependent charge excitations. O-AN sample contained an additional peak near the elastic peak independent of q , and the intensity of the elastic peak in the O-AN sample changed non-successive with the momentum. In contrast, the AS sample showed relatively higher intensity than the O-AN sample. Furthermore, by comparing the image plot results of AS and O-AN samples, the spectra weight of RIXS in AS sample is more concentrated.

In Fig. 2 (e), we plotted the ratio value of the integrated intensity of peaks corresponding to the hole-induced state and a hybridized state of the Cu upper Hubbard band with the O $2p$ states. Comparing them with the standard value of $\text{La}_{2-x}\text{Sr}_x\text{CuO}_4$ (LSCO) from the published report, it's clearly shown that the actual doping amount of strontium in both AS and O-AN samples is much lower than the chemometric value [6]. Meanwhile, the RIXS spectrum of $\text{La}_{2-x}(\text{Sr}, \text{Ba})_x\text{CuO}_4$ in a lightly doped region showed a momentum-independent behavior with a relatively weaker signal than the higher doping region, which would be one of the explanations for our results. However, from the theoretical part, the effect of apical oxygen is strongly correlated with the hopping parameter t , which may play an important role but is not taken into account. For the next step, the doping dependence of RIXS for the T^* phase cuprates is important [7].

REFERENCES

- [1] K. Ishii, *et al.* Phys. Rev. B **96**, 115148 (2017).
- [2] C. Jia, *et al.* Phys. Rev. X **6**, 021020 (2016).
- [3] K. Tsutsui and T. Tohyama, Phys. Rev. B **94**, 085144 (2016).
- [4] W. S. Lee, *et al.* Nature Phys. **10**, 883 (2014).
- [5] A. Greco, *et al.* Phys. Rev. B **94**, 075139 (2016).
- [6] C. T Chen, *et al.* Phys. Rev. Letter **66**, 104 (1991).
- [7] Y. Ohta, *et al.* Phys. Rev. B **43**, 2968 (1991).

Co $L_{3,2}$ -edge Soft X-ray Emission spectroscopy of $\text{La}_{0.6}\text{Sr}_{0.4}\text{CoO}_{3-\delta}$ for solid oxide fuel cells

Daisuke Asakura^{1,2}, Eiji Hosono^{2,3}, Tomohiro Ishiyama¹, Riyan Achmad Budiman¹, Haruo Kishimoto³, Kosuke Yamazoe⁴, Naoya Kurahashi⁴, Ralph J. Ugalino⁴, Hisao Kiuchi⁴, and Yoshihisa Harada^{2,4}

¹Research Institute for Energy Conservation, National Institute of Advanced Industrial Science and Technology (AIST)

²AIST-UTokyo Advanced Operando-Measurement Technology Open Innovation Laboratory, AIST

³Global Zero Emission Research Center, AIST

⁴Synchrotron Radiation Laboratory, The Institute for Solid State Physics, The University of Tokyo

Solid oxide energy devices including oxide-based all-solid-state Li-ion battery (LIB) are characteristic of the stability compared to energy devices with liquid systems. For example, solid oxide fuel cell (SOFC) is a well-known solid oxide energy device. SOFC is a fuel cell working at a high temperature (around 800 °C) with oxygen ion conduction. Oxygen in the air is supplied to the cathode (air electrode) and converted to O^{2-} ion with electrons from the circuit. The O^{2-} ions are transferred through a solid-state electrolyte and reach at the anode (fuel electrode). In the anode, the O^{2-} ions react with H_2 and are converted to H_2O with generating electrons, resulting in electricity generation. This is the operating principle of SOFC.

For the cathode of SOFC, 3d transition-metal oxides with the Perovskite structure are widely used. $\text{La}_{1-x}\text{Sr}_x\text{CoO}_{3-\delta}$ (LSC) is one of the prototypical cathode materials for SOFC while LSC has also been studied in the research field of strongly correlated electron systems. To further enhance the performance of LSC as the SOFC cathode, the electronic structure analysis for the Co 3d and O 2p orbitals is particularly important to understand the redox reaction and O^{2-} ion conduction mechanisms. Here, we employ the Co L -edge X-ray absorption spectroscopy (XAS) and X-ray emission spectroscopy (XES) for LSC utilizing experiences for LiCoO_2 which is a Co-oxide cathode material for LIB.

We conducted the Co $L_{3,2}$ -edge XAS and L_3 -edge XES measurements for a bulk LSC ($\text{La}_{0.6}\text{Sr}_{0.4}\text{CoO}_{3-\delta}$, made in AIST) by using HORNET spectrometer at BL07LSU, SPring-8. For XAS, total-electron-yield (TEY) and partial-fluorescence-yield (PFY) detection modes were employed. The energy resolution for the XES measurement was set to 240 meV at 780 eV.

Figure 1 shows the Co $L_{3,2}$ -edge TEY and PFY XAS spectra for the LSC. According to previous studies for LaCoO_3 and LiCoO_2 ,^{1,2} the XAS line shape for the TEY spectrum is assigned to be mainly Co^{3+} state while the peaks for 777-779 eV suggests a small

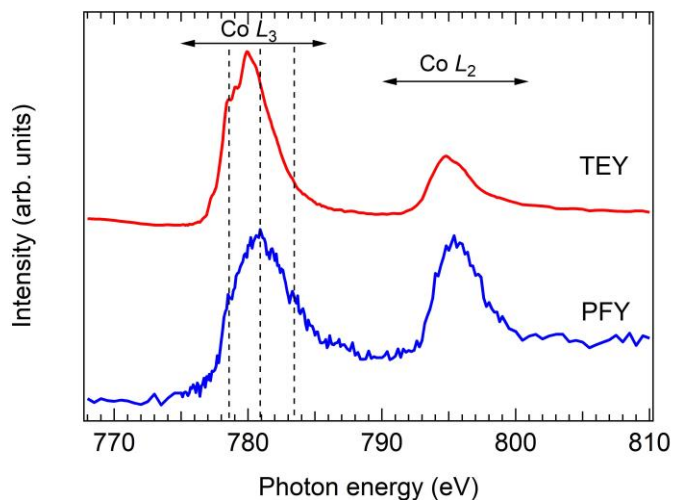


Fig. 1. Surface-sensitive TEY and bulk-sensitive PFY Co $L_{3,2}$ -edge XAS spectra for $\text{La}_{0.6}\text{Sr}_{0.4}\text{CoO}_{3-\delta}$.

amount of Co^{2+} should coexist. For the PFY spectrum, the highest point of Co L_3 edge shifted by +1 eV and the structure around 783 eV was enhanced, indicating that the oxidation state of the bulk region is higher than that near the surface.² Most likely, the Sr content and/or oxygen defect contributing to hole doping on the Co site should be suppressed near the surface. We selected three points characteristic of the Co L_3 -edge PFY spectrum (the dotted lines in Fig. 1) as the excitation energies for XES.

The XES results are shown in Fig. 2. For the 780.9-eV excitation, the broad structure around 775 eV should be of charge-transfer excitation. The structures from 776 to 780 eV should be of dd excitation, while the strong peak at 778 eV is ascribed to the fluorescence peak because the peak position is independent of the excitation energy. On the other hand, for a previous study of LaCoO_3 thin film, the peak position of fluorescence is lower in emission energy scale.¹ This difference between the LaCoO_3 thin film and LSC should correspond to that the oxidation state of Co is higher observed from the PFY XAS result. Similar energy shift of the fluorescence depending on the oxidation state has been also reported for the Co L_3 -edge XES for $\text{LiNi}_{0.65}\text{Co}_{0.25}\text{Mn}_{0.1}\text{O}_2$ (a cathode material for LIB).³ Thus, the XES spectra for LSC should include the component of Co^{4+} state in addition to that of the Co^{3+} state. The XAS and XES spectra will be analyzed with multiplet calculation. The relation between the electronic structure and the performance as a cathode for SOFC will be further investigated. Also, we will try the *operando* measurement with developing an all-solid-state-type *operando* cell for SOFC.

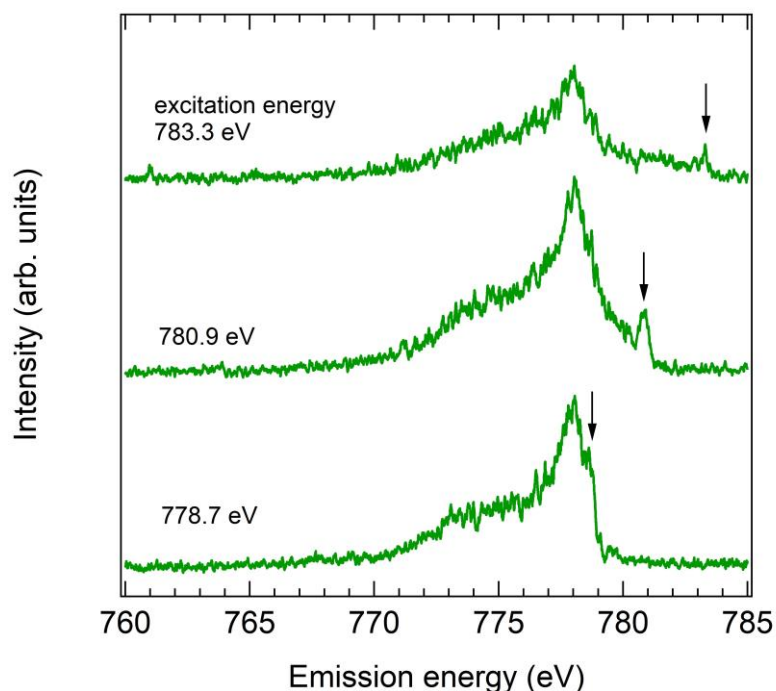


Fig. 2. Co L_3 -edge XES spectra for $\text{La}_{0.6}\text{Sr}_{0.4}\text{CoO}_{3-\delta}$. The arrows indicate the elastic scattering peaks.

REFERENCES

- [1] Y. Yokoyama *et al.*, Phys. Rev. Lett. **120**, 206402 (2018).
- [2] For example, W.-S. Yoon *et al.*, J. Phys. Chem. B **106**, 2526 (2002) and T. Mizokawa *et al.*, Phys. Rev. Lett. **111**, 056404 (2013).
- [3] H. M. Hollmark *et al.*, J. Electrochem. Soc. **157**, A962 (2010).

POSSIBLE ANAPOLE ORDER IN THE ANTIFERROMAGNETIC PHASE OF MULTIFERROIC CUO

Ryusuke MISAWA¹, Keito ARAKAWA¹, Hiroki UEDA², Jun MIYAWAKI³, Hisao KIUCHI⁴, Yoshihisa HARADA⁴, Yoshikazu TANAKA⁵, and Tsuyoshi KIMURA¹

¹*Dept. of Adv. Mater. Sci., The University of Tokyo*, ²*Paul Scherrer Institut*, ³*National Institutes for Quantum and Radiological Science and Technology*, ⁴*Synchrotron Radiation Laboratory, The Institute for Solid State Physics, The University of Tokyo*, ⁵*RIKEN SPring-8 Center*

The orbital current is characterized by a time-odd polar vector that corresponds to an anapole or toroidal moment [1]. It is proposed as the order parameter in the pseudo-gap phase of high- T_c cuprate superconductors and in the hidden ordered phase in some 5d transition-metal systems such as $\text{Sr}_2(\text{Ir,Rh})\text{O}_4$. Anapoles are formed by orbital currents between metal ions and ligands and between ligands as shown in Fig. 1. Symmetry breakings due to the orbital currents have been examined so far by several experimental techniques such as magneto-optical effects [2] and second harmonic generation [3]. Though some of the experimental results suggest the formation of anapole order, others do not support it [4]. In this study, we examined the presence of anapole order in antiferromagnetic CuO by using resonant x-ray diffraction (RXD) and resonant inelastic x-ray scattering (RIXS).

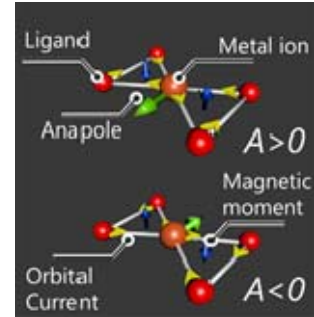


Fig.1. Schematic drawing of anapole moment induced by orbital currents.

CuO (space group: $C2/c$) exhibits successive magnetic transitions at $T_{N1}=213$ K and $T_{N2}=230$ K. At $T_{N1} < T < T_{N2}$, it shows an incommensurate (ICM) spiral magnetic order with the wavevector of $\mathbf{q}_{\text{ICM}} = (0.507, 0, -0.486)$. The spiral magnetic order induces spin-driven ferroelectricity [5]. The ferroelectricity disappears below T_{N1} where the magnetic structure transforms into a commensurate (CM) collinear antiferromagnetic one with the wavevector of $\mathbf{q}_{\text{CM}} = (0.5, 0, -0.5)$. Based on experimental results of circularly polarized resonant x-ray diffraction on CuO, the existence of anapole order induced by the orbital currents between copper and oxygen ions has been proposed in ref. [6]. However, some theoretical studies refute the interpretation [7], and no definitive conclusion has been reached on the proposed anapole-ordered state in CuO. The purpose of this study is to examine the anapole order and its domain state through scanning RXD and RIXS using circularly polarized x-rays.

We measured circularly polarized RXD and RIXS on a plate-shaped single crystal of CuO with the widest face parallel to the (10-1) plane. These measurements were carried out at BL07LSU, SPring-8. The incident x-ray energy was set near the Cu L_3 absorption edge. The incident x-ray beam was focused into ~ 34 μm (~ 5 μm) in the horizontal (vertical) direction at the sample surface position. RXD and RIXS at \mathbf{q}_{ICM} were measured in the ICM phase while those at \mathbf{q}_{CM} were obtained in the CM phase. The scattering geometry is illustrated in Fig. 2. The circular polarization dependence of these reflections and their spatial distributions were examined. We also examined the effect of electric fields on them. To apply the electric field, a pair of gold electrodes were deposited on the crystal surface (Fig. 2).

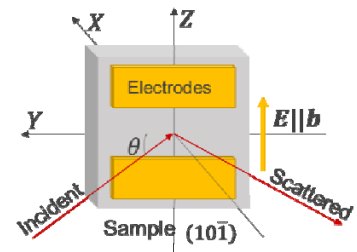


Fig. 2. Schematic drawing of scattering geometry.

The magnetic reflections in the two phases showed resonant enhancement at the energies around the Cu L_3 absorption edge (≈ 930 eV). In addition, they showed substantial circular polarization dependence. The circular polarization dependence in the ICM phase is explained by the spiral magnetic structure in the ICM phase while no confirmed mechanism

of that in the CM phase has not been provided yet. However, the electric field effect on the circular polarization dependence gives some clues for the understanding. Figure 3 shows the sample position dependence of the magnetic reflections in the ICM and the CM phases. For these measurements, the x-ray beam was scanned along the Z direction on the sample surface, and a positive or negative electric field was applied during the cooling of the sample and measurements. Figures 3(a) and 3(b) were obtained using the magnetic reflection with \mathbf{q}_{ICM} at 220 K (ICM phase) while Figs. 3(c) and 3(d) were taken using that with \mathbf{q}_{CM} at 200 K (CM phase). All the data shown in Fig. 3 were taken using incident x-rays with an energy of 929.7 eV. In all the measurements, a nearly uniform circular polarization difference over the sample area was observed. However, the sign of the circular polarization difference is reversed by a sign reversal of the electric field in both the phases. In addition, the sign of the circular polarization difference of the CM phase is the same as that of the ICM phase. At the present stage, we do not have a clear explanation for the origin of the circular polarization dependence in the CM phase. Clear supporting evidence of anapole order in the CM phase was not obtained. However, the similarity of the electric field effect observed in the ICM and the CM phases suggests that the order parameters of these two phases are correlated.

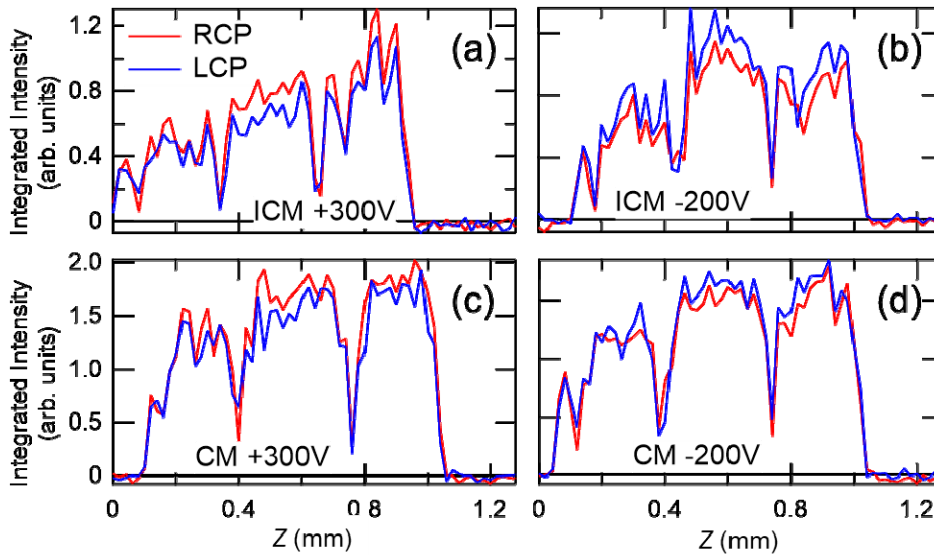


Fig. 3. Sample position dependence of magnetic reflection intensity measured using circularly polarized x-rays. (a,b) One dimensional scans of magnetic reflection at $\mathbf{q}_{\text{ICM}} = (0.507, 0, -0.486)$ in the ICM phase. (c,d) Those at $\mathbf{q}_{\text{CM}} = (0.5, 0, -0.5)$ in the CM phase. The scanning direction is along the Z direction. Measurements were carried out using right-circularly polarized (RCP) and left-circularly polarized (LCP) x-rays with energy corresponding to the $\text{Cu } L_3$ edge. The data of (a,c) were obtained in a positive electric field while those of (b,d) were taken in a negative electric field.

REFERENCES

- [1] C. M. Varma, *Phys. Rev. B* **55**, 14554 (1997).
- [2] Jing Xia, Elizabeth Schemm, G. Deutscher, S. A. Kivelson, D. A. Bonn, W. N. Hardy, R. Liang, W. Siemons, G. Koster, M. M. Fejer, and A. Kapitulnik, *Phys. Rev. Lett.* **100**, 127002 (2008).
- [3] L. Zhao, D. H. Torchinsky, H. Chu, V. Ivanov, R. Lifshitz, R. Flint, T. Qi, G. Cao & D. Hsieh, *Nat. Phys.* **12**, 32 (2016).
- [4] T. P. Croft, E. Blackburn, J. Kulda, Ruixing Liang, D. A. Bonn, W. N. Hardy, and S. M. Hayden, *Phys. Rev. B* **96**, 214504 (2017).
- [5] T. Kimura, Y. Sekio, H. Nakamura, T. Siegrist, and A. P. Ramirez, *Nat. Mater.* **7**, 291-294 (2008).
- [6] V. Scagnoli, U. Staub, Y. Bodenthin, R. A. de Souza, M. GarcíaFernández, M. Garganourakis, A. T. Boothroyd, D. Prabhakaran, and S. W. Lovesey, *Science* **332**, 696 (2011).
- [7] Y. Joly, S. P. Collins, S. Grenier, H. C. N. Tolentino, and M. De Santis, *Phys. Rev. B* **86**, 220101(R) (2012).

ELECTRONIC STRUCTURE ANALYSIS OF OXYFLUORIDE CATHODE OF ALL-SOLID-STATE FLUORIDE BATTERY USING RESONANT INELASTIC X-RAY SCATTERING

Kentaro YAMAMOTO¹, Datong ZHANG¹, Hisao KIUCHI², Jun MIYAWAKI²,
Tomoki UCHIYAMA¹, Toshiki WATANABE¹, Tsuyoshi TAKAMI¹,
Toshiyuki MATSUNAGA¹, Yoshihisa HARADA², Yoshiharu UCHIMOTO¹

¹*Graduate School of Human and Environmental Studies, Kyoto University*

²*Synchrotron Radiation Laboratory, The Institute for Solid State Physics, The University of Tokyo*

All-solid-state fluoride-ion battery is expected to be next-generation battery due to high electrochemical stability of F anion as charge carriers, as well as excellent theoretical energy densities which largely exceed those of conventional lithium-ion battery. Intercalation-type host materials, such as perovskite-, Ruddlesden–Popper⁻¹, etc., are particularly attractive owing to their high structural reversibility and F intercalation tolerance, compared with widely used conversion-type metal/metal fluoride systems (M/MF_x)². It is important for topotactic materials to have anionic vacancies surrounding cationic coordination centers as F⁻ intercalation sites; therefore, those with low-coordination environment of cations can be promising host materials for F (de)intercalations. In this study, we introduced Ca_{0.85}CuO₂ as high-energy cathode material for all-solid-state fluoride-ion battery with an infinite-layer-related modulated chain structure. Slightly distorted square planar [CuO₄] provide sufficient rooms for F⁻ intercalation. Considering the large contributions to charge compensation from redox of oxygen in Ca_{0.85}CuO₂, the electronic structure of O was investigated by resonant inelastic X-ray scattering (RIXS) techniques.

Ca_{0.85}CuO₂ was synthesized via solid-state reactions. CaCO₃ and CuO were ground, pelletized and calcined at 800 °C for 20 hours with immediate regrinding afterward. The calcining and regrinding were repeated several times until single phase was acquired. Electrochemical properties were studied using bulk-type cells, with La_{0.9}Ba_{0.1}F_{2.9} (LBF), Ca_{0.85}CuO₂/LBF/ vapor grown carbon fiber (VGCF) composite, and Pb/PbF₂/LBF/VGCF composite as solid electrolyte, cathode and anode, respectively. Ex situ Cu K-edge, Cu L_{2,3}-edge and O K-edge XAS data were acquired in the partial fluorescence yield (PFY) mode at BL14B2 and BL27SU in SPring-8. Resonant inelastic X-ray scattering (RIXS) measurements were performed at BL07LSU in SPring-8 using a grazing flat-field type high resolution soft X-ray emission spectrometer. The measurements were conducted under vacuum and the samples were transferred from an Ar-filled glove box without exposure to air.

The Ca_{0.85}CuO₂ cathode showed high capacity of 890 and 630 mAh g⁻¹ in initial charging and discharging in the cut-off range of -1.5 to 3.0 V, respectively, corresponding to approx. 4.3 and 3.1 F⁻ intercalation/deintercalation (Figure 1). A large irreversible capacity in initial discharging might be related to the loss of oxygen or irreversibility of oxygen redox. After controlling the oxidation state of oxygen by cut the initial capacity to that of 3.0 F intercalation, the initial coulombic efficiency was greatly enhanced. According to XAS results, in initial charging process, oxygen redox is the major contributor to charge compensation. In initial discharging, both Cu and O were reduced; the uncomplete reduction of O species was highly possible to be the origin of low coulombic efficiency of initial cycle. In RIXS results of charged Ca_{0.85}CuO₂F_{3.0} sample, the peaks at the emission energy of 523.5 eV with an incident photon energy of 530.9 eV revealed the generation of O-O bond. This was also supported by the vibrations at 529 to 531 eV (energy loss of -2.0 to 0 eV), as well as the corresponding frequency of the first vibrational level (0.2 eV, approx. 1600 cm⁻¹)³. In addition, it is also highly possible that Cu²⁺ in pristine-state Ca_{0.85}CuO₂ could be further oxidized to

higher valency upon charging since the number of intercalated F anions exceeds the capability of oxygen redox, which requires more decisive evidence.

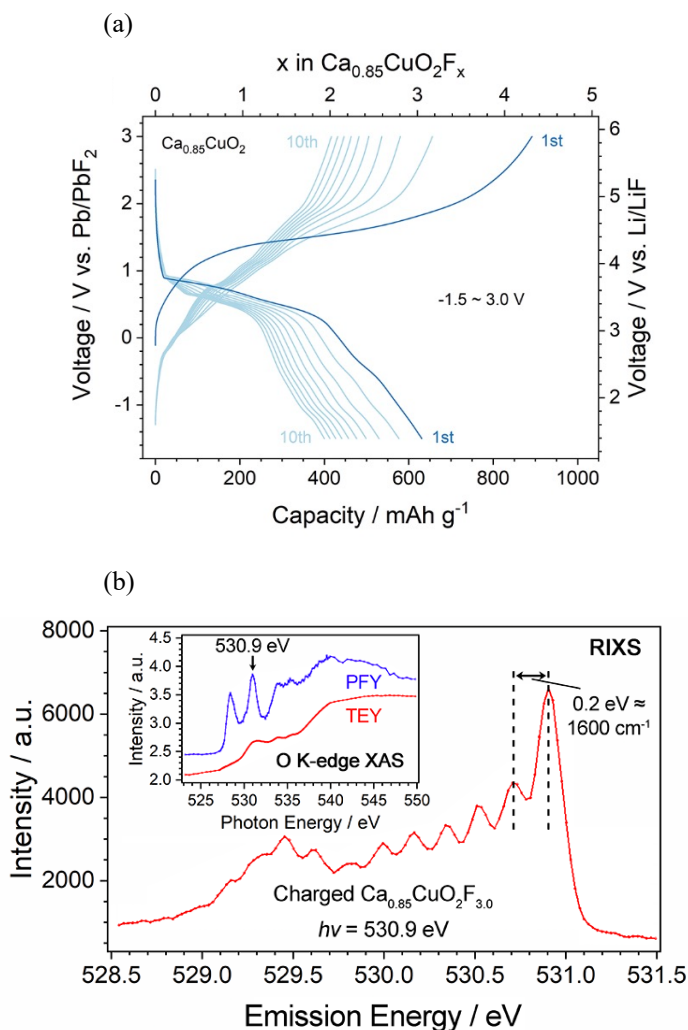


Fig. 1 (a) Charge-discharge profile of $\text{Ca}_{0.85}\text{CuO}_2$ cathode material with various cut-off conditions. (b) O K-edge XAS (inset) and corresponding RIXS results of charged $\text{Ca}_{0.85}\text{CuO}_2\text{F}_{3.0}$ sample.

REFERENCES

- [1] M. A. Nowroozi, K. Wissel, J. Rohrer, A. R. Munnangi, and O. Clemens, *Chem. Mater.* 2017, **29**, 3441–3453.
- [2] M. Anji Reddy and M. Fichtner, *J. Mater. Chem.* 2011, **21**, 17059–17062.
- [3] R. A. House, U. Maitra, M. A. Pérez-Osorio, J. G. Lozano, L. Jin, J. W. Somerville, L. C. Duda, A. Nag, A. Walters, K.-J. Zhou, M. R. Roberts, and P. G. Bruce, *Nature* 2020, **577**, 502–508.

OPERANDO AMBIENT PRESSURE PHOTOELECTRON SPECTROSCOPY OF CHEMICAL REACTION ON THE FUNCTIONALIZED BASAL AND EDGE SURFACES OF MoS₂

F. OZAKI, Y. CHOI, H. Li, Y. SAWAGUCHI, S. TANAKA, K. MUKAI, M. HORIO, I. MATSUDA and J. YOSHINOBU

The Institute for Solid State Physics, The University of Tokyo

Introduction

Molybdenum disulfide (MoS₂) is a layered substance that exists as a natural mineral (Fig. 1), and recently it is expected to be used for various applications such as field-effect transistors and photoelectric devices due to its unique physical properties [1]. In addition, it has been used as a catalyst for a long time. For example, Co-MoS₂ has been used industrially as a hydrodesulfurization catalyst to remove sulfur from oil [2]. Thus, the MoS₂ surface is a various catalytic reaction field involving hydrogen, and it is important to understand the interactions between the hydrogen molecules and MoS₂ surface.

It is known that the exfoliated MoS₂ (0001) basal surface is inert to the dissociation of molecular hydrogen, and the active site as a catalyst is mainly the edge of MoS₂. Tanaka and Okuhara have reported that the edge site plays a vital role, by comparing the catalytic activity of an un-cut MoS₂ with that of a MoS₂ cut by a pair of scissors to increase the edge area [3]. So far, the edge sites have only been studied by microscopic observation using scanning tunnelling microscopy and theoretical first-principles calculations due to their small scale and the difficulty of preparing a defined surface [4,5]. Therefore, it is a challenging issue to observe the chemical and electronic states of edge sites. In particular, the mechanisms of these reactions at the edge surfaces have not been elucidated yet. Therefore, we have conducted experimental observation of the chemical and electronic states of the edge surface using an ambient pressure photoelectron spectroscopy (AP-XPS).

Experimental

In this study, we prepared the edge surfaces of MoS₂ which were sharply cut perpendicular to the MoS₂ basal plane by ultrashort laser pulse processing at Kobayashi Laboratory in LASOR of The Institute for Solid States Physics (ISSP). In the case of mechanical cutting, possible metal contaminations from a scissors and edge-sagging by scission are inevitable. Laser processing does not cause edge-sagging and produces a fine edge surface (Figure 2). The spot size of SPring-8 BL07LSU is about 50 × 10 μm², and thus the edge can be selectively illuminated by synchrotron radiation. The incident photon energy was 655 eV and all measurements were carried out at room temperature. The MoS₂ single crystals were heated in ultra-high vacuum (UHV) to remove impurities, and the clean edge surfaces were observed by

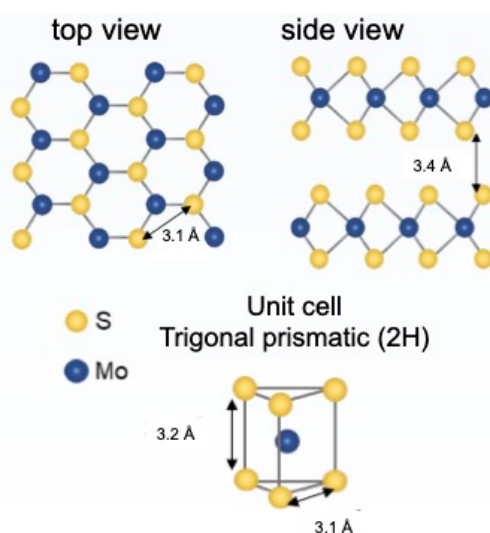


Figure 1 Structural model of MoS₂

XPS at SPring-8 BL07LSU. AP-XPS measurements were performed in hydrogen gas in order to investigate the reactivity of the edge surface with hydrogen molecules.

Results and discussion

The edge surface of MoS₂ was observed by XPS in UHV in order to investigate the changes caused by heating treatment. Figure 3 shows a series of Mo 3d XPS spectra in UHV. The Mo 3d spectrum of an “As installed” sample (Figure 3: blue) shows small oxidized components at ~230.9 and ~234.0 eV on the high binding energy side of the main Mo 3d_{5/2} and 3d_{3/2} peaks, respectively. After annealing at 700 K for 30 min, the oxidized components decreased in intensity. After further annealing at 700-800 K for 220 min, a shoulder appeared at ~228.3 eV. This shoulder component may be assigned to Mo²⁺ indicating a less coordinated state (missing S) than Mo⁴⁺ in the bulk MoS₂.

The annealed sample was then transferred and installed at an AP-cell to investigate the reaction between the unsaturated Mo sites and hydrogen gas. The shoulder peak of Mo 3d XPS that appeared after the heat treatment decreased with the introduction of hydrogen (not shown here). This may be due to the dissociative adsorption of hydrogen at the less-coordinated Mo sites at the edge. The details of the present study will be reported elsewhere.

In this study, we have succeeded in directly measuring the electronic state of the coordinatively unsaturated Mo sites on the edge surface which was prepared by ultrashort pulse laser processing. AP-XPS results have shown that these sites are involved in the adsorption.

ACKNOWLEDGMENTS

We thank Dr. S. Tani (Kobayashi laboratory in LASOR, ISSP) for preparing the edge surface of MoS₂ by ultrashort pulse laser processing. The AP-XPS measurements using synchrotron radiation were performed at SPring-8 BL07LSU as joint research between the Synchrotron Radiation Research Organization and The Institute for Solid State Physics, The University of Tokyo (Proposal No. 2021B7432).

REFERENCES

- [1] M. Chhowalla *et al.*, Nat. Chem. **5**, 263-275 (2013).
- [2] Y. Okamoto, Catal. Today **132**, 9 (2008).
- [3] K.-I. Tanaka, T. Okuhara, J. Catal. **78**, 155-164 (1982).
- [4] F. Besenbacher, J.V. Lauritsen, J. Catal. **403**, 4-15 (2021).
- [5] M. Sun *et al.*, J. Catal. **233**, 411-421 (2005).

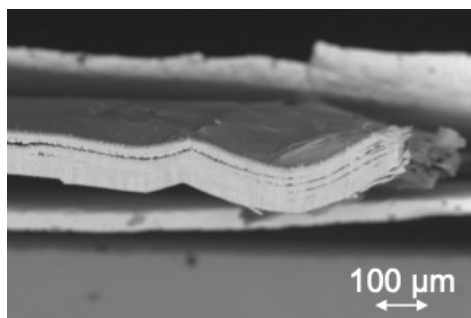


Figure 2 A secondary electron microscopy image of the MoS₂ edge prepared by ultrashort laser pulse processing

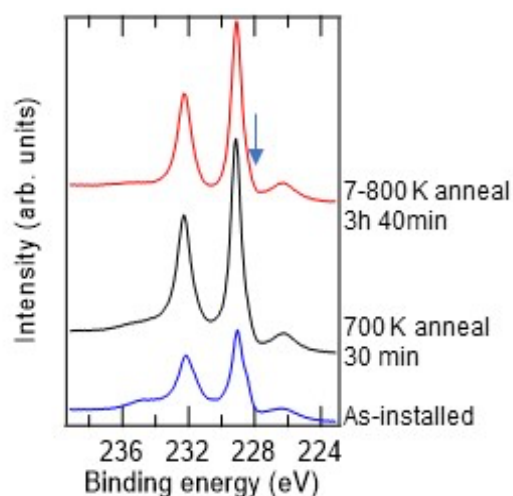


Figure 3 A series of Mo 3d XPS spectra of the MoS₂ edge surface in UHV.

ELECTRONIC STATE ANALYSIS OF EARTH-ABUNDANT FE-AL-SI THERMOELECTRIC (FAST) MATERIALS USING SCANNING PHOTOELECTRON MICROSCOPY

Yoshiki TAKAGIWA¹, Shunsuke TSUDA¹, Naoka NAGAMURA^{1,2}, Asako YOSHINARI^{1,3}, Shingo TAKEZAWA^{1,3}, Kenta OISHI^{1,2,3}, Kentaro FUKU⁴, Wenxiong ZHANG⁵

¹National Institute for Materials Science (NIMS), Tsukuba, Ibaraki, Japan.

²PRESTO, Japan Science and Technology Agency, Honcho, Saitama, Japan.

³Tokyo University of Science, Katsushika, Tokyo, Japan

⁴Tohoku University, Sendai, Miyagi, Japan

⁵The University of Tokyo, Kashiwa, Chiba, Japan

To develop new thermoelectric materials that are non-toxic and low-cost with sufficient power output for autonomous power supplies to drive sensor devices, in particular, at a low-temperature region below 400 K, we performed materials screening of ternary Fe-Al-Si system using first-principles band structure calculations [1,2]. We found that the ternary τ_1 -Fe₃Al₂Si₃ phase forms a narrow bandgap of ~0.2 eV near the Fermi level and has shown potential as a novel thermoelectric material (FAST materials: Fe-Al-Si Thermoelectric Materials). We have demonstrated that the Al/Si ratio fine-tuning could control its conduction type and enhance the power factor without chemical substitutions [2]. Relatively large power factors were obtained for both p- and n-type thermoelectric materials below 400 K, which possessed high oxidation resistance and excellent mechanical properties [3]. Recently, we enhanced the power factor at mid-temperatures using machine-learning-assisted synthesis and evaluation [4]. We have established a mass production process for FAST materials and succeeded in the bonding technology to build a small-sized and highly integrated thermoelectric power generation module: the operation of temperature/humidity sensors and wireless transmission was performed [5]. Furthermore, we have succeeded in a synthesis of composition graded samples to find an optimized composition using a bulk combinatorial method with diffusion couple and mapping measurements [6]. Both theoretical [7,8] and experimental works [6,9] are essential to enhancing the thermoelectric properties. The remaining issue is to investigate the electronic structure experimentally and obtain the additional route for better thermoelectric performance.

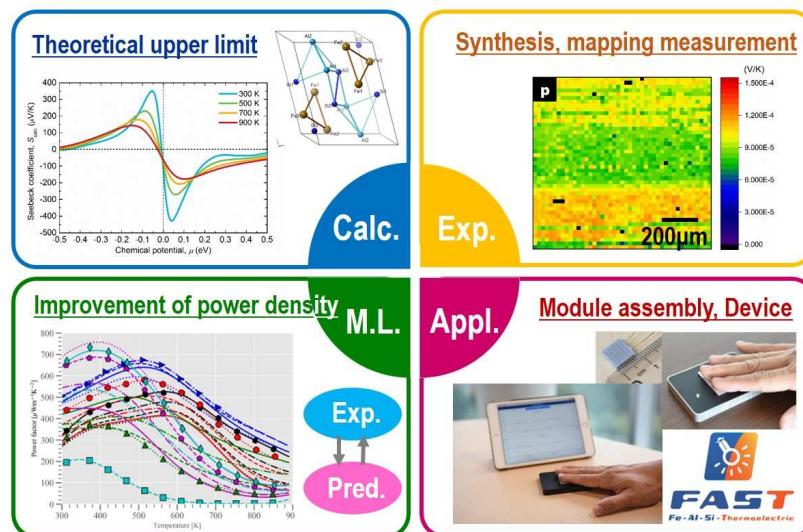


Fig. 1 Research and development of FAST materials using experiments, theoretical calculation, machine learning, and module development.

In this experiment, based on the FAST material of τ_1 -Fe₃Al₂Si₃, (1) bulk samples of n-type and p-type semiconducting FAST materials with high thermoelectric properties and (2) composition gradient samples were prepared. The core level spectra (Fe 2p, Al 2p, Si 2p, C 1s, O 1s) and valence spectra were measured in each sample. At first, a sample was prepared, as shown in Fig. 2(a). Since severe surface oxidation and carrier charging were observed, the bulk sample was fixed with silver paste, and gold was deposited, as shown in Fig. 2(b). And then made it break in a vacuum.

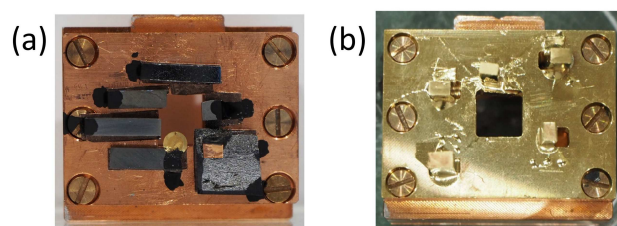


Fig. 2 Photos of sample holders.

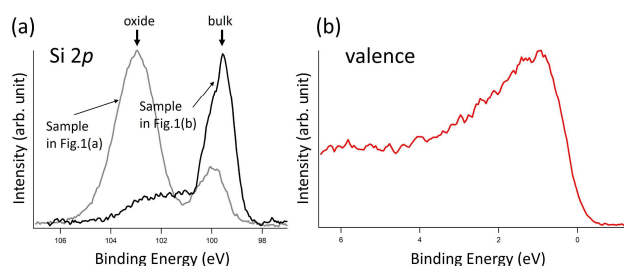


Fig. 3 (a) Si 2p core level spectra (b) valence spectrum.

The beamline used BL07LSU, which has high energy resolution in the soft X-ray region, and the device used a multi-dimensional operando photoelectron spectroscopy named "operando 3D nano-ESCA", which has a high spatial resolution (~ 70 nm). For the single composition bulk samples of FAST material, the spectrum derived from the oxide is significantly reduced in the spectrum measured by the sample holder of Fig. 1(b), as compared with the spectrum measured by the sample holder of Fig. 1(a). It was found that a spectrum derived from a bulk sample excluding the influence of surface oxidation was successfully obtained, as shown in Fig. 3(a). For the composition graded sample, the core level spectrum derived from the dopant could not be obtained with sufficient intensity; therefore, the sample preparation and measurement sample were considered major issues for the next beam time.

The valence spectrum is also measured, and the valence band maximum in each sample is specified from the rising edge, as shown in Fig. 3(b). Based on the results obtained this time, we will acquire data to quantitatively evaluate the difference in thermoelectric characteristics/transport characteristics and the core level spectrum/valence spectrum of FAST material samples at the next beam time.

REFERENCES

- [1] Y. Takagiwa, Y. Isoda, M. Goto, and Y. Shinohara, *J. Therm. Anal. Calorim.* **131**, 281 (2018).
- [2] Y. Takagiwa, Y. Isoda, M. Goto, and Y. Shinohara, *J. Phys. Chem. Solids* **118**, 95 (2018).
- [3] Y. Takagiwa and Y. Shinohara, *Scripta Mater.* **172**, 98 (2019).
- [4] Z. Hou, Y. Takagiwa, Y. Shinohara, Y. Xu, and K. Tsuda, *ACS Appl. Mater. Interfaces* **11**, 11545 (2019).
- [5] Y. Takagiwa, T. Ikeda, and H. Kojima, *ACS Appl. Mater. Interfaces* **12**, 48804 (2020).
- [6] Y. Takagiwa, Z. Hou, K. Tsuda, T. Ikeda, and H. Kojima, *ACS Appl. Mater. Interfaces* **13**, 53346 (2021).
- [7] Z. Hou, Y. Takagiwa, Y. Shinohara, Y. Xu, and K. Tsuda, *J. Phys.: Condens. Matter* **33**, 195501 (2021).
- [8] N. Sato and Y. Takagiwa, *crystals* **11**, 388 (2021).
- [9] A. K. Srinithi, H. Sepehri-Amin, Y. Takagiwa, and K. Hono, *J. Alloys Compds.* **903**, 163835 (2022).

ANALYSIS OF WATER STRUCTURE OF THERMORESPONSIVE POLYMER MODIFIED INTERFACE

Kenichi NAGASE¹, Naoya KURAHASHI², Hisao KIUCHI², Yoshihisa HARADA²

¹*Faculty of Pharmacy, Keio University*

²*Synchrotron Radiation Laboratory, The Institute for Solid State Physics, The University of Tokyo*

Introduction

Thermoresponsive polymer, poly(*N*-isopropylacrylamide)(PNIPAAm), exhibits temperature-responsive hydration and dehydration across lower critical solution temperature (LCST) of 32°C [1]. Using the property, PNIPAAm have been utilized various types of biomedical applications, such as drug delivery systems, bioseparation materials, and cell culture substrates [2,3]. However, the detailed investigation of the hydration property of PNIPAAm on substrate were not investigated, although the PNIPAAm hydration/dehydration in solution state was already clarified. In this study, we investigate the water structure in the modified PNIPAAm on substrate using high-resolution soft X-ray emission spectroscopy (XES).

Experiments

a) Sample preparation

PNIPAAm was synthesized by activator regenerated by electron transfer atom transfer radical polymerization (ARGET-ATRP) [4]. NIPAAm was dissolved in 2-propanol and water mixed solvent. Then, ATRP catalyst, CuCl₂, tris[2-(dimethylamino)ethyl]amine, and L-ascorbic acid, were added in the solution. ARGET-ATRP of NIPAAm was performed at 25°C for 16 h. After the polymerization, the prepared PNIPAAm was purified by dialysis and freeze drying. The prepared PNIPAAm was dissolved into methanol, and the PNIPAAm solution was casted to Au-coated SiC membrane. The methanol in casted solution was evaporated in a drying oven.

b) Soft X-ray emission spectroscopy (XES) measurement

Soft XES measurement of PNIPAAm cast film was performed by using ultra-high resolution soft X-ray emission spectrometer HORNET [5] installed at the SPring-8 BL07LSU. Water vapor was supplied by steam-generation equipment, and nitrogen was used as the carrier gas. Ultrapure water was used as the water source. Moisture was passed over the PNIPAAm casted film and then drained from the outlet port. Relative humidity was ranged from 0%-100%. Temperature was set at 20°C and 40°C.

Results

The water content of the PNIPAAm modified cast film was estimated at various relative humidity (Figure 1). Water content λ (water molecule/oxygen atom) increased with increasing the relative humidity, because the adsorbed water on PNIPAAm increased with relative humidity. Higher water content of the PNIPAAm was observed at 20°C compared to that of 40°C, because of the temperature-dependent hydration of PNIPAAm. The XES spectra at 20°C and 40°C were observed (Figure 2). Higher peak intensity was observed at 20°C compared to that at 40°C. The result indicates that the adsorption of water molecules to carbonyl group of PNIPAAm is enhanced at 20°C compared to that at 40°C, which is attributed to the temperature-dependent hydration of casted PNIPAAm on the substrate.

The XES measurement can observe the temperature-dependent adsorption of water molecules onto the carbonyl group of the modified PNIPAAm on the substrate. The obtained results can be utilized for the design of the PNIPAAm modified substrate.

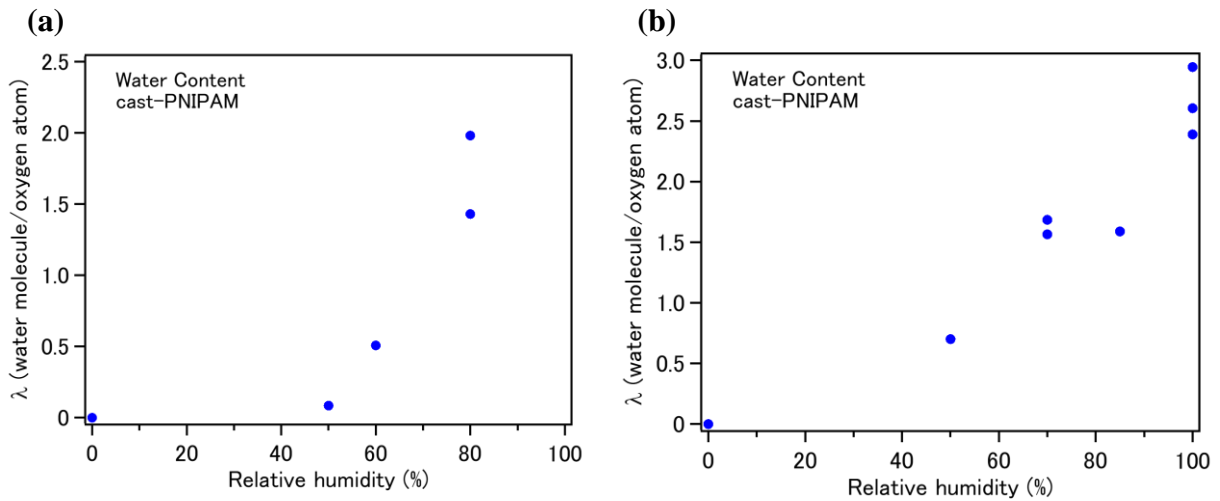


Fig.1 Water content (water molecule/oxygen atom) in PNIPAAm cast film at various relative humidity (a) at 20°C and (b) at 40°C.

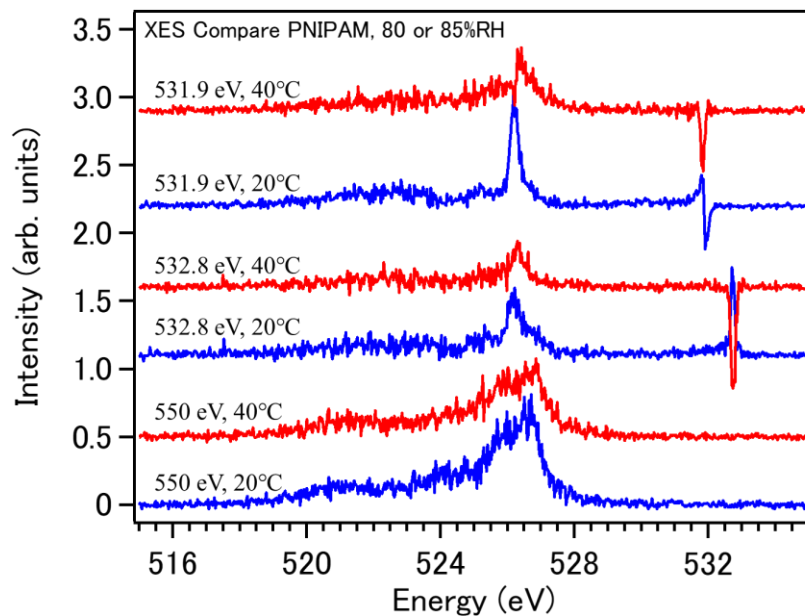


Fig.2 XES spectra of PNIPAAm cast film at 20°C and 40°C.

REFERENCES

- [1] Heskins, M., Guillet, J. E., *J. Macromol. Sci. A* 2: 1441-1455, (1968)
- [2] Nagase, K., Yamato, M., Kanazawa, H., Okano, T., *Biomaterials* 153: 27-48, (2018)
- [3] Nagase, K., *Advances in Colloid and Interface Science* 295: 102487, (2021)
- [4] Nagase, K., Shimura, M., Shimane, R., Hanaya, K., Yamada, S., Akimoto, A. M., Sugai, T., Kanazawa, H., *Biomaterials Science* 9(3): 663-674, (2021)
- [5] Yamazoe, K., Higaki, Y., Inutsuka, Y., Miyawaki, J., Cui, Y.-T., Takahara, A., Harada, Y., *Langmuir* 33(16): 3954-3959, (2017)

RESONANT INELASTIC X-RAY SCATTERING SPECTROSCOPY OF CU-PROTEINS

Kentaro FUJII^{1,2}, Jun MIYAWAKI², Naoya KURAHASHI³, Hisao, KIUCHI³,
Yoshihisa HARADA³, Motoyasu ADACHI¹, Akinari YOKOYA¹

¹*Institute for Quantum Life Science, National Institutes for Quantum Science and Technology*

²*Advanced Synchrotron Radiation Centre, National Institutes for Quantum Science and Technology*

³*Synchrotron Radiation Laboratory, The Institute for Solid State Physics, The University of Tokyo*

Amicyanin and Azurin are classified as Class I TICu protein amicyanin, whose axial ligand is the sulfur atom of methionine. Both protein molecules share the asymmetric structure of four amino acids, Met, Cys, and two His, as the ligand for the copper atom (Fig. 1). Azurin contains an additional second axial ligand in addition to methionine in one axial position, as seen in the difference in distance to the oxygen atom. Crystallographic analysis has revealed that this asymmetry differs by a few percent between azurin and amicyanin¹. Their redox potentials differ by about 30 mV at pH 8.0. In addition, both amino acid mutations have been introduced by genetic recombination technology, and significant redox potential changes of 500 mV or more have been observed when amino acid substitutions are introduced directly or indirectly at the copper atom. Especially, the changes of nearly 100 mV have been reported even at positions more than 10 Å from the copper atom. In order to reveal these phenomena, we examined the resonant inelastic soft X-ray scattering (RIXS) measurement of these solutions.

Both proteins were prepared as recombinant proteins expressed in *E. coli* using BL21 (DE3) and pET24a vector. The samples were purified with Ni-sepharose and ion-exchange columns. The ion-exchange columns used were HiTrap Q XL columns for amicyanin and HiTrap SP XL columns for azurin. The final solutions (~ 3mM) were

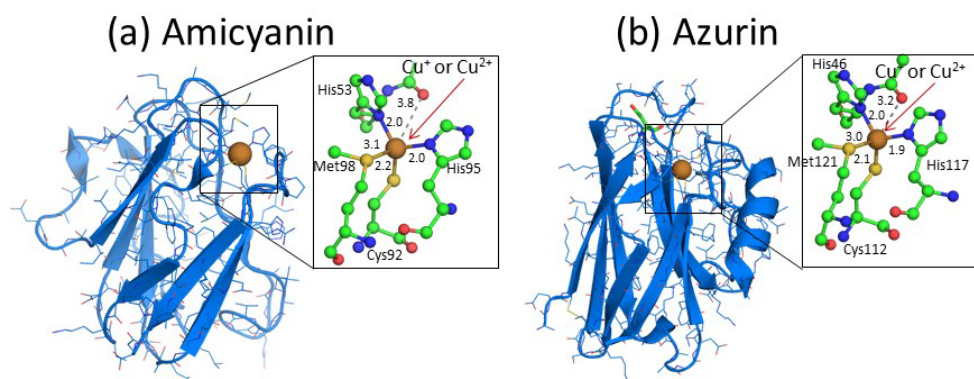


FIG 1 Molecular picture of (a) amicyanin and (b) azurin. The structures around Cu-atom are superimposed. Cu-atom is surrounded by Met, Cys and two His.

obtained by dialyzing in 20 mM Tris-HCl buffer (pH 8.0). The measurement the protein solutions was performed using a solution cell under ambient pressure by circulating the sample solution. To avoid oxidation of the sample, the circulated solutions were bubbled with nitrogen gas during the measurement.

Soft X-ray emission spectra around Cu-Ledge and resonant inelastic scattering emission spectra after Cu-L pre-edge resonance excitation (931 eV excitation) were shown in Figure 2 and Figure 3, respectively. These spectra were obtained using a high-resolution soft X-ray emission spectrometer HORNET² installed at the end of the BL07LSU of SPring-8. The apparent peak structures of each spectrum were observed. In order to assign these peak structures, we are currently performing density functional theory simulations using a model molecule that imitates the coordination of amino acids around Cu. N.J. Fowler et al., predicted reduction potentials for several Cu proteins containing mutants using DFT calculation. In the future, we plan to perform RIXS spectroscopy on mutants with different amino acid residues surrounding Cu or different pH to obtain information on the correlation between the structure and electronic properties around Cu. This information regarding copper proteins has useful for general use in biotechnology, such as enzyme-catalyzed fuel cells or valorization of lignocellulosic biomass.

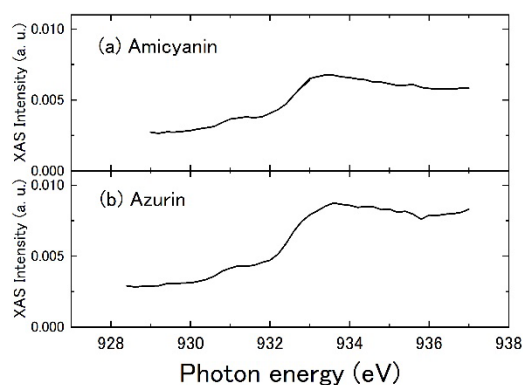


FIG 2 Cu *L*-edge XAS of (a) amicyanin and (b) azurin with 20mM Tris-HCl buffer solutions (~3mM).

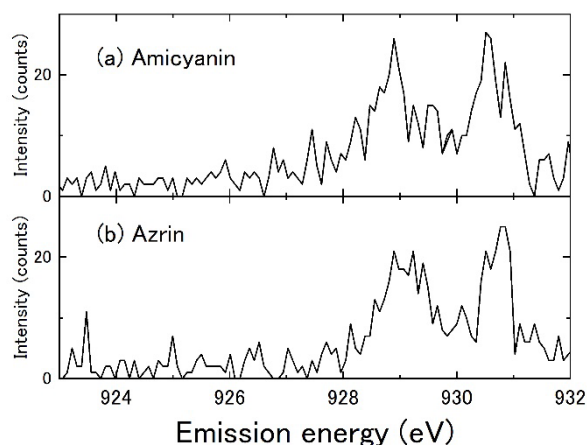


FIG 3 Cu *L*-edge RIXS spectra of (a) amicyanin and (b) azurin with 20mM Tris-HCl buffer solutions (~3mM).

REFERENCES

- [1] N.J. Fowler, C.F. Blanford, J. Warwicker, S.P. de Visser, Chem. Eur. J. 12 (2017) 15436-15445.
- [2] Y. Harada et al., Rev. Sci. Instrum. 83 (2012) 013116.